

Computational Modeling of the Electrical Sensing Properties of Single Wall Carbon Nanotubes

by

Shawn D. Bair

Submitted in Partial Fulfillment of the Requirements

for the Degree of

Master of Science in Engineering

in the

Chemical Engineering

Program

YOUNGSTOWN STATE UNIVERSITY

August 2015

Computational Modeling of the Electrical Sensing Properties of Single Wall Carbon Nanotubes

Shawn D. Bair

I hereby release this thesis to the public. I understand that this thesis will be made available from the OhioLINK ETD Center and the Maag Library Circulation Desk for public access. I also authorize the University or other individuals to make copies of this thesis as needed for scholarly research.

Signature:

Shawn D. Bair, Student

Date

Approvals:

Dr. Pedro Cortes, PhD, Thesis Advisor

Date

Dr. Mike Crescimanno, PhD, Committee Member

Date

Dr. Donald Priour, PhD, Committee Member

Date

Dr Sal Sanders, Associate Dean of School of Graduate Studies

Date

ABSTRACT

Carbon nanotubes (CNTs) are an ever expanding field of research due to their unique physical and electrical properties since their discovery. Based on how they are cut and rolled from a graphene sheet, carbon nanotubes can exhibit semiconducting or metallic behavior. These electrical properties can change dramatically as molecules bond to their highly reactive surfaces. These property changes make CNTs very promising materials for bio-chemical sensing applications.

In this work, the electrical properties of (8,0) single-wall carbon nanotubes in the presence of NO_2 and NH_3 have been studied and modeled using density functional tight binding theory and non-equilibrium Greens functions through the DFTB+ program. Explanation of how this initial modeling was performed, as well as literature review, results, and analysis are all contained within this work.

The results obtained on the modeled CNTs exposed to NO_2 and NH_3 as dopant molecules under vacuum conditions appear to show conventional semiconductor behavior when varying an applied gate voltage. Here, NO_2 is shown to function as a hole donating molecule, decreasing the conduction of the system, while NH_3 is shown to function as an electron donating molecule, causing opposite effects on conductivity.

The DFTB+ modeling program used demonstrates fast calculation times for reasonably sized systems and small bias voltages used. Using this program and the work performed herein, larger, more complicated systems with more and different dopant molecules could easily be modeled.

Contents

Chapter 1. Introduction	1
1.1 Carbon Nanotubes: History and Overview	1
1.2 Electron Transport and Technological Background	4
1.2.1 P and N type Semiconductors	5
1.2.2 Field Effect Transistors in Electrochemical sensors	5
1.3 Modeling	7
1.3.1 Hartree-Fock Approximation	7
1.3.2 Density Functional Theory	10
1.4 Relation to Conduction and Transistors	11
1.5 Introduction to Non-Equilibrium Green's Functions (NEGF)	12
1.6 Objectives	12
1.7 Organization	13
Chapter 2. Literature Review	14
2.1 Density Functional Theory (DFT) Studies on Bare CNTs	14
2.2 Studies on the CNT Sensing Capabilities	16
2.3 Studies on Multiple CNT Systems	21
Chapter 3. Modeling	23
3.1 Density Functional Tight Binding Theory (DFTB)	23
3.2 Non-Equilibrium Green's Functions	28
3.3 Poisson Solver	30

3.4 Single Wall Carbon Nanotube (SWCNT) Generation and Visualizing.....	31
Chapter 4. Modeling Methodology	33
4. 1 Computer Set-Up	33
4. 2 Modeling Set-Up	34
4.3 Contact Sample Input.....	44
4.3.1 Geometry	44
4.3.2 Driver and Hamiltonian	46
4.3.3 Remaining Simulation Settings.....	47
4. 4 Device Sample Input.....	48
4. 4.1 Geometry and Initial Settings.....	48
4.4.2 Driver and Hamiltonian	50
4.3.3 Poisson Solver	50
4.3.4 Gate Settings.....	51
4.3.5 Green's Function's Solver	51
Chapter 5. Results and Discussion.....	53
5.1 NO ₂ Distance Variation	53
5.2 Gate Potential Variation.....	54
5.3 Effects of NO ₂ and NH ₃ on the Conductivity of CNTs	57
6. Conclusions	60
References	62

List of Figures

Figure 1.1 A schematic representation of graphene folding to form CNTs, where a and b represent unit vectors, and T represents the axis of the CNT. [2]	2
Figure 1.2 Schematic Representation of the different types of CNTs [3]	2
Figure 1.3 Comparison of an sp^2 , $ p_z$ and a bent, hybridized $ hpz^*$ carbon. The p_z orbital of the hybridized carbon is larger on the exterior side. [6].....	3
Figure 1.4 Geometry of the curved cap of a CNT. [5]	4
Figure 1.5. Schematic representation of the Fermi energy and energy bands in different materials. The larger the band gap, the more resistant to conduction the material tends to be. [7]	5
Figure 1.6. Schematic representation of a carbon nanotube field effect transistor. The CNTs form a conducting bridge between the source and drain electrodes. [10]	6
Figure 2.1. Density of states of a (7,7) armchair CNT. The lack of any band gap, normally indicated by the Density of States (DOS) going to 0, shows that this CNT has metallic electrical properties. [14]	14
Figure 2.2. Simulated DFT results for CNTs. The Fermi levels are demonstrated by the vertical EF lines. Pure (14,0) CNT (left) shows a band gap and semiconducting properties, while Ti-adsorbed (14,0) (right) shows no band gap and metallic electrical properties. [16]	15
Figure 2.3. A graph from Kong et al's study on the effects of gases on CNT conductance. The current is plotted against the gate voltage. The NO_2 treated samples needed a much higher back-gate voltage to lower the current to approximately zero. [19]	17
Figure 2.4. Conductance of a CNT vs time after being exposed to different gases. The conductance rapidly changes an order of magnitude when exposed to NO_2 and decreases 1-2 orders of magnitude when exposed to NH_3 ,.....	18
Figure 2.5. Conductivity versus gate voltage of CNTs after a) annealing and b) exposure to oxygen. The red data points represent the CNT protected by PMMA, and maintains its n-type properties, while the unprotected CNT changes to p-type upon exposure to oxygen.[20]	19

Figure 2.6. Current as a function of gate voltage for a device with untreated SWCNTs (a) and SWCNTs functionalized with polythyleneimine (b). P type behavior is demonstrated in (a), and n type in (b). [22]	20
Figure 2.7 Reaction of a SWCNT FET to a stream of saturated ethanol vapor. [23]	21
Figure 2.8. CNTs (top) become deformed as they move closer than 0.34 nm [24].....	22
Figure 2.9. Graph of resistance vs distance between CNT axes. The intrinsic resistance stays constant until deformation begins at $d = D$ (tube diameter) + Van der Waal distance (0.34 nm) [24]	22
Figure 2.10. Total junction resistance of two deformed CNTs as a function of the junction angle. Resistance increases rapidly by orders of magnitude as the tubes approach a parallel orientation [24].	22
Figure 2.11. The resistance (left axis), and stress (right axis), are plotted as functions of the volume fraction of randomly orientated CNTs. The increase of compression and CNT volume fraction led to a decrease in resistance, likely due to reduced separation distance.	23
Table 3.1 Energy integrals for crystal in terms of two-center integrals.[33]	25
Figure 3.1. A visualization of an (8,0) SWCNT with an NO ₂ molecule approximately 2.18 Å from the nanotube surface [45].	32
Figure 4.1 VirtualBox software used to create a virtual machine for running a Linux operating system.	33
Figure 4.2 The structure of the "bin" folder where the dftb+ program was placed to allow it to be more easily executed.	34
Figure 4.3. The necessary SKF files for an NO ₂ doped CNT calculation.	35
Figure 4.4. The "GS" and "contacts" folders necessary for any transport calculation.....	36
Figure 4.5. Completed folder for a gated NO ₂ doped CNT.	37
Figure 4.6. A terminal may be opened by right clicking in the folder and selecting "Open Terminal Here".	38
Figure 4.7 Opened Terminal window, where the "dftb+" command has to be issued.....	38
Figure 4.8 Terminal window containing a completed contact calculation resulting from dftb+ command issued in figure 4.7.....	39
Figure 4.9. Calculation folder after contact calculation.	40

Figure 4.10. Output file "detailed.out" for source contact calculation	41
Figure 4.11. DFTB + NEGF calculation proceeding, alternating between computing density matrix and Poisson equation. (Image taken from nearly finished calculation).....	42
Figure 4.12 DFTB+NEGF calculation completed	43
Figure 4.13. The "detailed.out" file from DFTB+NEGF calculation using the device input file.	44
Figure 5.1 Representation of the system for distance variation simulations. S and D stand for source and drain respectively. In these simulations, current was measured at increasing separation distance between the CNT and NO ₂ molecule.	53
Figure 5.2 Current through a (8,0) SWCNT as a function of the distance of distance of NO ₂ molecule from surface. The equilibrium distance for the molecule is 2.3 Angstroms	54
Figure 5.3. Visualization of either NH ₃ or NO ₂ doped system.	55
Figure 5.4. Effect of Gate Variation on Current flow through (8,0) CNT. NO ₂ Doped CNT shows lowest conduction under positive gate voltage, and highest under negative voltage due to hole donation.....	57
Figure 5.5 Current through an (8,0) SWCNT as a function of bias voltage in the presence of a -7 V planar gate. The presence of NO ₂ improves conductivity, while NH ₃ slightly reduces it, until a switch to electron charge carrier conduction at 1 V bias.	58

Chapter 1. Introduction

1.1 Carbon Nanotubes: History and Overview

Since being thrust into the spotlight by Iijima [1] in 1991, Carbon Nanotubes (CNTs) have been a focus of chemical, mechanical, and electrical research for their unique properties, such as their incredible tensile strength and high electrical conductivity. For having such useful properties, a CNT's structure is conveniently simple. Carbon nanotube structure consists of a rolled sheet of graphene, which is itself a flat, one atom thick sheet of sp^2 bonded carbon atoms. These strong carbon bonds give the CNTs a very high tensile strength (over 100 GPa) property, allowing a CNT to have a length much larger than its diameter, making it a good candidate for structural materials. CNTs can be classified by how a graphene sheet would be folded to produce the CNT. Figure 1.1 shows a schematic representation of a graphene sheet, here the endpoints of the vector \mathbf{C} represent the atoms that will be brought together to form the CNT with its axis in the T direction (orthogonal to \mathbf{C}). The value of the vector \mathbf{C} , typically shown as $\mathbf{C} = n\mathbf{a} + m\mathbf{b}$, determines the properties of CNTs and therefore divides the CNTs into three different types: Armchair, where $n = m$; Zig Zag, where $m = 0$; and Chiral, where $n \neq m$ (see figure 1.2).

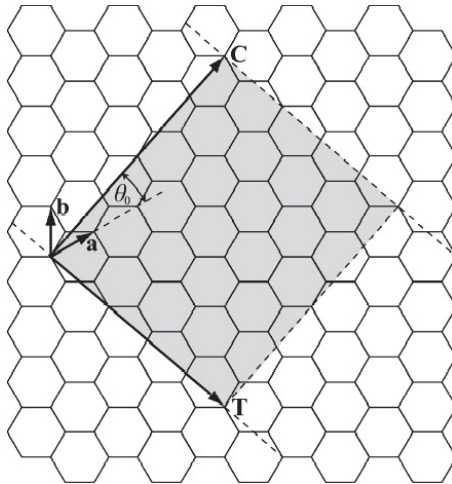


Figure 1.1 A schematic representation of graphene folding to form CNTs, where a and b represent unit vectors, and T represents the axis of the CNT. [2]

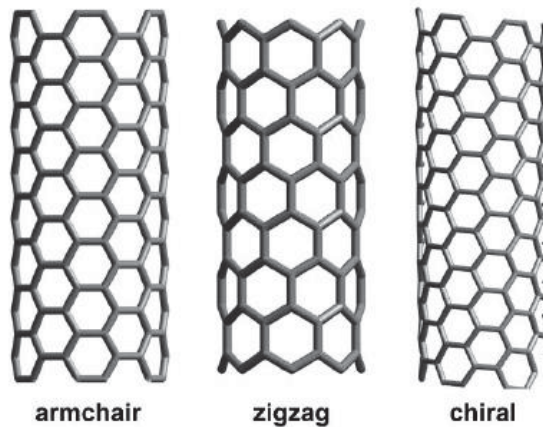


Figure 1.2 Schematic Representation of the different types of CNTs [3]

The atomic configuration of the CNTs has a large effect on their structural features, especially the electrical properties. Armchair CNT's for example, always exhibit metallic electrical properties, while zigzag and chiral exhibit semiconducting properties with an electrical fluctuation depending on the angle of the vector C . The reason for this variation in properties is related to how the graphene Brillouin zone is folded by the CNT rolling [4].

In addition to the types of nanotubes mentioned previously, CNTs can be either single walled or multi walled. Single walled CNT (SWNT) diameters tend to range

between 0.4 and 2.0 nm. Above and below these diameters, the nanotube arrangement is no longer energetically favorable for the carbon. Large diameter nanotubes are more stable when they are a layer of a multi walled nanotube (MWNT), which consists of many concentric SWNTs. The outer diameter of a MWNT is capable of being many times greater than a SWNT [5].

One of the most useful properties of CNTs is the reactivity of their exposed pi bonding surfaces. The curvature of these surfaces causes increased reactivity, as the electron cloud of the pi orbital is forced more to the outside of the tube (see figure 1.3). Thus, the rounded ends of a CNT are especially reactive (see figure 1.4). Many atomic structures are capable of bonding to a CNT, and when they do, they change the electrical properties of the CNT. This change in electrical properties can be measured, by a drop in voltage for example. By functionalizing a CNT to be more selective to one certain molecule, the CNT can be used as a sensor to detect specific molecules [6].

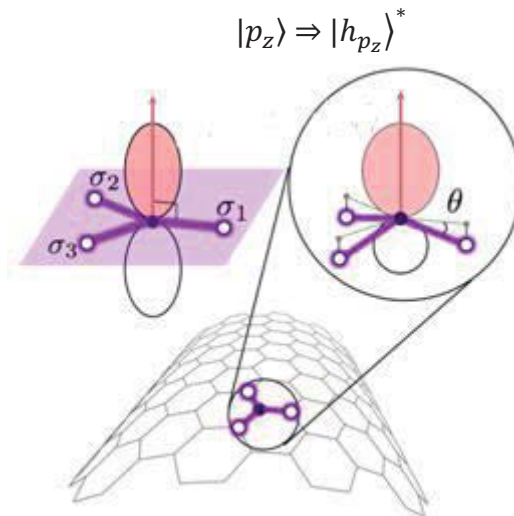


Figure 1.3 Comparison of an sp^2 , $|p_z\rangle$ and a bent, hybridized $|h_{p_z}\rangle^*$ carbon. The p_z orbital of the hybridized carbon is larger on the exterior side. [6]

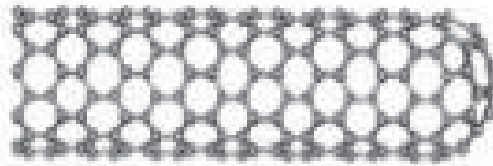


Figure 1.4 Geometry of the curved cap of a CNT. [5]

1.2 Electron Transport and Technological Background

As stated earlier, CNTs exhibit metallic and semiconducting electrical behavior. This is due to the value of the Fermi energy of the electron cloud of the CNT. The Fermi energy is the energy up to which the electron states are filled. The filled states immediately beneath the Fermi energy level are referred to as the valence band, while the empty states above are referred to as the conduction band. A metal has nearly no gap between the Fermi energy level and the conduction band. This means that electrons can easily be transported throughout the system without having to "jump" to a much higher energy state, as is the case in an insulator. A semiconductor has a small gap between the Fermi energy and the conduction band (see figure 1.5). [7]

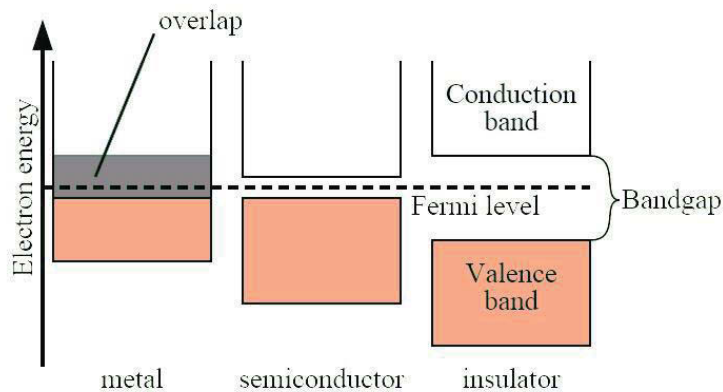


Figure 1.5. Schematic representation of the Fermi energy and energy bands in different materials. The larger the band gap, the more resistant to conduction the material tends to be. [7]

1.2.1 P and N type Semiconductors

When used as conductive material, the CNT provides charge carriers to allow for current flow from one end of the CNT to the other. If the CNT has an excess of electrons, due to electron donating groups bonding to it, then it is an n-type semiconductor which uses electrons as charge carriers. If the CNT has a shortage of electrons, it is a p-type semiconductor which uses holes, empty electronic states in the valence band behaving much like positively charged electrons, as charge carriers. The large surface area and reactivity of CNTs allows for many groups to bond to it, allowing a CNT that does not conduct charge very well initially to conduct very well in the presence of an electrophilic or nucleophilic molecule that turns the CNT into an n-type or p-type semiconductor. As mentioned earlier, by tailoring a CNT to selectively bind to certain molecules, the change in its electrical properties can be utilized to detect specific analytes of interest.

1.2.2 Field Effect Transistors in Electrochemical sensors

CNT's large surface area and small diameter makes them useful as conducting bridges in field effect transistors (FETs). This bridge connects source and drain electrodes which are

mounted on a silicon dioxide layer over a silicon base (see figure 1.6). A gate contact under the silicon layer is also frequently present to help control current flow. Initially, the fermi level of the system would be close to its unperturbed thermal equilibrium position. When a positive potential difference is placed over the source-drain connection, the source contact's fermi level rises above that of the drain's. Electrons, seeking lower energy levels, flow across the CNT to the drain. Enough of a negative voltage would cause the reverse to happen, with electrons flowing from the drain to the source. Placing a positive gate voltage over the system has the effect of lowering the energy levels in the bridging material, making the conduction band easier to access for electrons. An opposite effect happens with a negative gate voltage [8]. For a CNT to conduct charge carriers effectively, either electrons or holes, it must have available bands for the charge carriers to flow through [9]. Indeed, the presence of molecules can change the conductivity of a CNT, which make them a potential core sensing material for the detection of bio-chemical analytes.

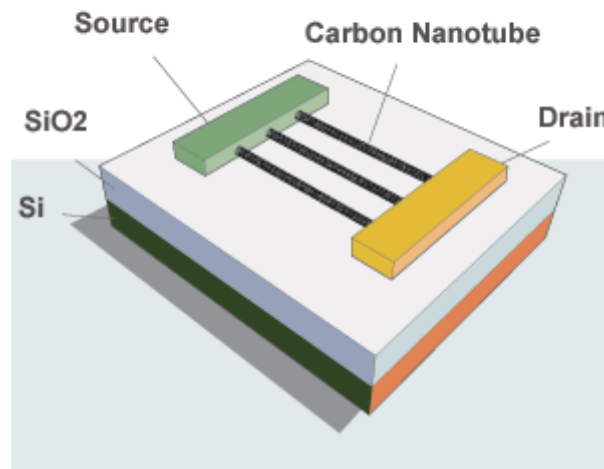


Figure 1.6. Schematic representation of a carbon nanotube field effect transistor. The CNTs form a conducting bridge between the source and drain electrodes. [10]

1.3 Modeling

1.3.1 Hartree-Fock Approximation

As sensing experiments on CNTs can be an expensive and time consuming activity, much interest has been shown in modeling the electrical-sensing properties of CNTs. Discovering how the electrical properties change as molecules bind to the CNT or as the environment changes, as well as investigating how the CNT can be functionalized to perform most optimally for detecting desired materials, are crucial steps for the development of CNT based sensors.

To find the conductance through a CNT bridge, it is necessary to know about the electrons present in the CNT, as conduction is the movement of charge carriers through the system. So, it is desired to find the wavefunction of the electrons using the Schroedinger Equation.

$$H\varphi = E\varphi \quad (1.1)$$

Where H is the Hamiltonian operator, φ is the wavefunction of the electrons, and E is the total energy (of non moving atomic nucleus.) The wave function incorporates dependence on the electron and ionic positions [11].

From the Schroedinger equation, it is possible to calculate the energy of the electrons as a function of atomic positions (r_i). The force and acceleration of the electrons can then be obtained by

$$F_i = m_i a_i = -\nabla_{r_i} E(\{r_j\}) \quad (1.2)$$

Here, the force on the i th atom in the molecule, F_i which is equal to the mass, m_i , times resulting acceleration, a_i , is equal to the gradient of the total energy.

This approach is called *ab initio*, or first principles in molecular dynamics modeling since no assumptions are made at the outset as to the molecular structure, and all observables of

interest emerge from the calculation itself. While these few equations may look simple, the apparent simplicity is deceptive, and the process of solving them as written is so excessively computationally intensive as to render it impossible without making approximations, a few of which are examined below.

The first approximation used to simplify this problem is through the Born-Oppenheimer Approximation, in which one calculates wave functions and molecular energies under the assumption that the ions are stationary. This is a reasonable approximation in many instances because the atomic nuclei are more than three orders of magnitude more massive than the electrons, 1.67×10^{-27} kg per proton opposed to 9.11×10^{-31} , and so move much more slowly as compared to the electrons since acceleration for a given force is inversely proportional to mass. This removes the kinetic energy and potential energy (which for a given set of nuclear positions is now a constant) of the ions. The Born-Oppenheimer Hamiltonian is then expressed as

$$H_{BO} = -\sum_{i=1}^n \left[\frac{\hbar^2 \nabla^2}{2m_e} \right] - \sum_{i,j}^{n,N} \left[\frac{Z_i e^2}{|\rho_i - r_j|} \right] + \sum_{i < j}^n \left[\frac{e^2}{|\rho_i - \rho_j|} \right] \quad (1.3)$$

With the first summation being the kinetic energy of the electrons, the second being the potential energy of each atomic core with each electron, and the third, the potential energy from electron-electron reactions. The variable n is the number of electrons, and N is the total number of atoms in the system. In principle, one could solve this equation by numerical means. However, even in the context of the Born-Oppenheimer approximation, the electron wavefunction is a 3n-dimensional function, which proves too computationally intensive to integrate over for anything larger than small n.

To reduce the complexity of the task and solve for physical observables of interest, the mean field approximation is used, which assumes that the total wave function of the electrons is simply the product of the wave function of each electron.

$$\psi(\rho_i) = \varphi_1(\rho_1)\varphi_2(\rho_2) \dots \varphi_n(\rho_n) \quad (1.4)$$

Substituting this into the Schrodinger equation reduces a multiparticle eigen-equation into n single particle equations and leads to the Hartree equation for one of the electrons wavefunction φ_j , as:

$$\left[-\left[\frac{\hbar^2 \nabla^2}{2m_e} \right] - \sum_i^N \left[\frac{Z_i e^2}{|\rho_j - r_i|} \right] + \sum_{i \neq j}^n e^2 \int \left[\frac{|\varphi(\rho')|^2}{|\rho - \rho'|} d^3 \rho' \right] \right] \varphi_j = E' \varphi_j \quad (1.5)$$

Where, the third term represents the interaction of one electron with the average of all other electrons. Here, one electron is moving around still ions in an average field of other electrons. In this manner, the Hartree approximation results in a system with n 3D integral functions that need to be solved.

However, the electrons in the Hartree equation are distinguishable, meaning that swapping a pair of them changes the total wave function. As fermions, swapping two electrons should only change the wave function by a factor of -1 since electrons are in fact indistinguishable, with the -1 factor resulting from the antisymmetrization requirement imposed by the Pauli Exclusion Principle. The implementation of this requirement, in conjunction with the Hartree mean field picture leads to the Hartree-Fock method, where the total electron wave function is given by a Slater Determinant where antisymmetrization arises automatically from the mathematical structure of the matrix determinant:

$$\psi = \frac{1}{\sqrt{N!}} \begin{bmatrix} \varphi_1(\rho_1) & \varphi_2(\rho_1) & \cdots & \varphi_n(\rho_1) \\ \varphi_1(\rho_2) & \varphi_2(\rho_2) & \cdots & \varphi_n(\rho_2) \\ \vdots & \vdots & \ddots & \vdots \\ \varphi_1(\rho_n) & \varphi_2(\rho_n) & \cdots & \varphi_n(\rho_n) \end{bmatrix} \quad (1.6)$$

Thus, the total energy in Hartree-Fock then, given by the expectation value of the Hamiltonian, is expressed as:

$$\begin{aligned}
\langle H \rangle = & \sum_{i=1}^n \int d^3r \varphi_i^*(\rho) \left[\frac{\nabla}{2m_e} - \sum_j \frac{Z_j e^2}{|\rho - r_j|} \right] \varphi_i(\rho) + \sum_{i < j}^n \int d^3\rho d^3\rho' \frac{e^2 |\varphi_i(\rho)|^2 |\varphi_j(\rho')|^2}{|\rho - \rho'|} \\
& - \sum_{i < j}^n \int d^3\rho d^3\rho' \frac{e^2 \varphi_i^*(\rho) \varphi_j^*(\rho') \varphi_i(\rho') \varphi_j(\rho)}{|\rho - \rho'|}
\end{aligned} \tag{1.7}$$

The third sum in equation 1.7 represents something known as the exchange energy, which results from two electrons of the same spin not being able to share an orbital, and is purely quantum mechanical in nature.[11]

1.3.2 Density Functional Theory

A more common approach, and a technique which improves on the Hartree Fock mean field approach by accounting for correlations among electrons, used to model CNT's today is the density functional theory. This model, first developed by Hohenburg and Kohn in 1964 [10,12], states that the ground state electron wave function is a function of the total electron density:

$$n(r) = \int d^3r_2, d^3r_3, \dots, d^3r_n |\psi(r, r_2, \dots, r_n)|^2 \tag{1.8}$$

This theory states that the density that minimizes the energy is the ground state density

$$E_0 = \langle \psi_0(n_0) | H | \psi_0(n_0) \rangle = E(n_0) \tag{1.9}$$

where the 0 subscript indicates ground state. This energy is expressed by the following equation,

$$E(n) = T_s(n) + U_H(n) + V_{ext}(n) + E_{xc}(n) \tag{1.10}$$

where $T_s(n)$ is a kinetic energy term, U_H is the potential Hartree term, V_{ext} is the energy from the interaction with atoms, and E_{xc} is the exchange and correlation energy. Kohn and Sham found a solution to this equation in the following single particle form

$$\left[-\frac{\hbar^2}{2m} \nabla^2 + v_{ext}(r) + v_H(r) + v_{xc}(r) \right] \varphi_i = \epsilon_i \varphi_i \tag{1.11}$$

Here, the first term represents the kinetic energy, and the other variables are related to those with the same subscripts shown in equation 1-10. The electron density is then able to be calculated as

$$n(r) = \sum |\varphi_i(r)|^2 \quad (1.12)$$

This calculated value can then be compared, and used in place of the first guessed density, and then repeated iteratively until convergence is reached and the energy minimized. The exact value of E_{xc} is unknown but is approximated by the local density approximation

$$E_{xc} = -\frac{3q^2}{4} \left(\frac{3}{\pi}\right)^{\frac{1}{3}} \int d^3r \rho(r)^{\frac{4}{3}} \quad (1.13)$$

where q is the charge of an electron.

1.4 Relation to Conduction and Transistors

After finding the electron wave functions, base energy, and band gaps, these terms are related to the physical characteristics of a system such as conductivity. A relatively simple way of performing this is through the following equations based off of Green's Functions.

$$I = \frac{q}{\hbar} \int dE D(E - U) * \frac{\gamma_1 \gamma_2}{\gamma_1 + \gamma_2} * (f_1 - f_2) \quad (1.14)$$

$$N = \int dE D(E - U) * \frac{\gamma_1 f_1 + \gamma_2 f_2}{\gamma_1 + \gamma_2} \quad (1.15)$$

$$U = U_L + U_0(N - N_0) \quad (1.16)$$

Here, I is the current, q , is the electron charge, and D , is the density of states of the material in the bridge of the transistor. The constants γ_1 and γ_2 represent the quality of the contacts used at each end, f_i is the fermi level at the contacts, U_L is the potential in FET channel with no charge, U_0 is the change in potential with addition of one electron, N is the number of electrons, and N_0 is the original number of electrons. This is an iterative solution, as U and N depend on each other. The more in depth form of these equations, the non-equilibrium Green's Functions

equations (NEGF), involves operators and hence, essentially changes most of these terms into matrices [7].

1.5 Introduction to Non-Equilibrium Green's Functions (NEGF)

The use of Non-Equilibrium Green's Functions (NEGF) in this work consists of making an initial estimate for a self consistent potential, and then solving for the charge density matrix by using NEGF with DFTB calculations. Where the charge density, ρ , is defined as

$$\rho = \frac{1}{2\pi i} \int_{-\infty}^{+\infty} dE G^<(E) \quad (1.17)$$

Here $G^<$ represents the electron-electron correlation matrix. Through a calculated charge density, a new potential V is calculated using the Poisson equation, $\nabla^2 V = -\rho/\epsilon_0$. This potential is subsequently used to find another refined charge density through the NEGF calculations, and this process continues iteratively until convergence is achieved and the current can be calculated [13].

1.6 Objectives

The present research work will establish the initial platform of computational simulation work using Density Functional Tight Binding Theory and Non-equilibrium Greens Functions for the electrical response of SWCNTs in the presence of simple gases. In more detail, this thesis will:

1. Implement and evaluate preliminary modeling methods to aid in researching the electrical properties of carbon nanotubes for potential sensing applications.
2. Simulate the conductivity of single SWCNTs in the in the presence of simple gases and potential fields.

1.7 Organization

This work is divided into six chapters. Chapter One contains a brief summary of carbon nanotubes' properties and uses, modeling, and the objectives and organization of this thesis. Chapter 2 provides a more detailed description of CNTs, their history, discovery, past research, and current applications and their use as sensors. Chapter 3 provides details on molecular modeling and examines several models which are currently used. Chapter 4 examines the technical set up of the modeling performed in this work. Chapter 5 discusses the results of the modeling carried out in this thesis. Lastly, Chapter 6 contains a summary of this investigatory work.

Chapter 2. Literature Review

The synthesis of CNTs was first described by Sumio Iijima in 1991 [1]. In this work, through the arc-discharge evaporation of carbon in an argon filled container, Iijima was able to form coaxial tubes of graphite sheets. These multi-walled carbon nanotubes contained as many as 50 nanotubes sharing the same center. Using electron micrographs, he was also able to determine that the separation distance between the tubes was the same as the observed between graphene layers in bulk graphite, 0.34 nm [1].

2.1 Density Functional Theory (DFT) Studies on Bare CNTs

The electronic properties of a (7,7) armchair CNT were examined by Salehi and Gharbavi [14] using the Density Functional Theory (DFT) framework. The method utilized for these calculations was full potential-linearized augmented plane wave DFT with a generalized gradient approximation. This method consists of dividing space into spherical regions around the nuclei and the remaining interstitial regions. In the spherical regions, the basis sets are the Schrodinger Equation solutions, while the interstitial region's basis set is simply plane waves. As can be seen in Figure 2.1, the obtained graph of the density of states shows the expected result of a zero band gap for the metallic (7,7) armchair CNT.

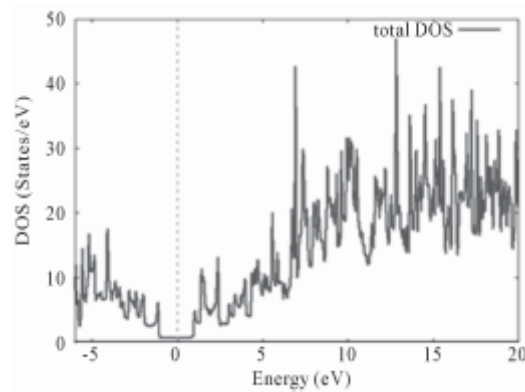


Figure 2.1. Density of states of a (7,7) armchair CNT. The lack of any band gap, normally indicated by the Density of States (DOS) going to 0, shows that this CNT has metallic electrical properties. [14]

Further modeling work on the conduction properties of CNTs was performed by Tetik et al [15], who used the SIESTA ab initio modeling package to perform DFT calculations through the local density approximation to model several nanotubes. In addition to reinforcing Salehi and Gharbavi's results [14], metallic electrical properties were observed in the (6,0) zigzag CNT, while a band gap of 0.5022 eV was found for the (7,0) CNT, suggesting semiconducting properties as expected. Also, they observed that whilst the (6,2) CNT has a band gap of 0.8291 eV, which the researchers call large compared to the other observed CNTs, the (6,3) CNT has a very small gap of 0.0488 eV, making it quasimetallic in its electrical properties [15].

Further DFT modeling studies were performed by Louis et al [16], on the effects of titanium chain adsorption on CNTs. Their work showed that the semiconducting CNT became metallic in nature after titanium adsorption and the metallic CNT became semiconducting (see figure 2.2). These changes were attributed to transfer of charge from the titanium to the CNT. This serves as a further example of the large effects on conductivity that exposure to various molecules can have on a CNT [16].

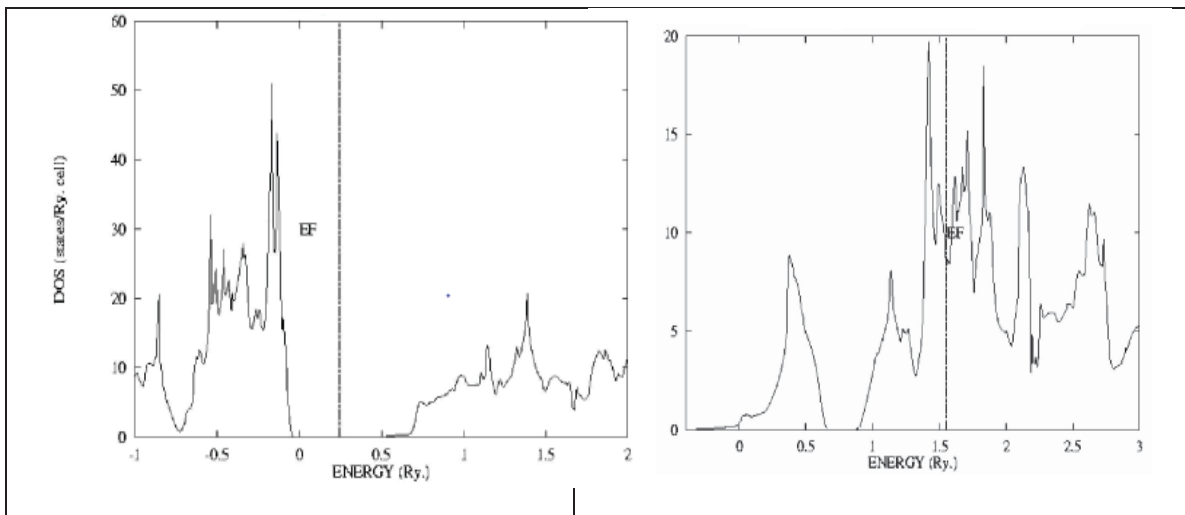


Figure 2.2. Simulated DFT results for CNTs. The Fermi levels are demonstrated by the vertical EF lines. Pure (14,0) CNT (left) shows a band gap and semiconducting properties, while Ti-adsorbed (14,0) (right) shows no band gap and metallic electrical properties. [16]

More evidence of the effectiveness of DFT for determining CNT band structure and state density can be seen in Kuganathan's study [17], where DFT framework using local density approximation and norm conserving pseudopotentials for core electrons was applied. This DFT method is quite similar to the one used in the present study, so the results obtained are useful for comparison to any state densities that would be calculated by the method in this study [17].

These studies demonstrate the accuracy of DFT based modeling systems for determining the base electrical properties of CNTs. These methods are made further appealing due to the cost of CNTs for experimentation. As of May 2015, 1 gram of >70% SWCNTs is priced at \$618 from Sigma-Aldrich, with a gram of all (7,6) SWCNTs priced at \$928 [18]. Modeling can help to provide initial information to lower the amount of experiments needed, and thus the expense of research. Further studies, both experimental and computational, have been performed on the topic related to the electrical properties of a CNT in a large variety of physical conditions.

2.2 Studies on the CNT Sensing Capabilities

Kong et al [19] studied the effects of NO_2 and NH_3 exposure on the resistance of semiconducting SWCNTs. The SWCNTs were grown on a SiO_2/Si substrate and then placed in sealed glass flasks through which NO_2 (2 to 200 ppm) or NH_3 (1% in Ar or air at a flow rate of 700 ml/min) was flowed through. They observed large changes in the conductance of the CNTs after ten minutes of exposure, as shown in figure 2.3. Here, the CNT was determined to be a hole-doped semiconductor, due to an increase in conductivity when exposed to the hole-donating NO_2 gas, resulting in an increase in charge carriers.

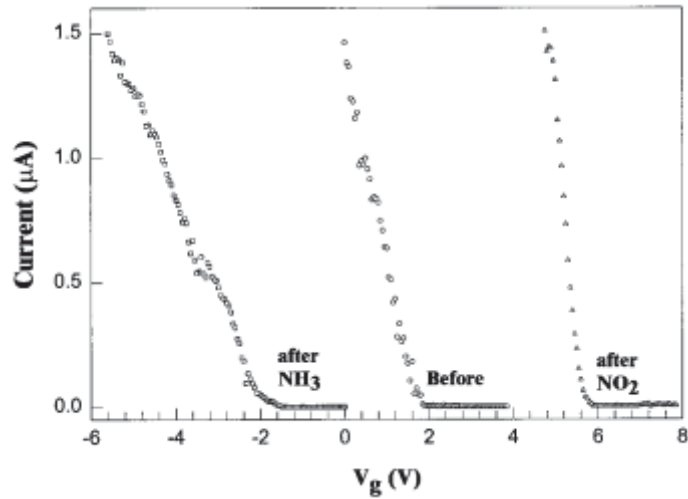


Figure 2.3. A graph from Kong et al's study on the effects of gases on CNT conductance. The current is plotted against the gate voltage. The NO₂ treated samples needed a much higher back-gate voltage to lower the current to approximately zero. [19]

Kong et al observed that the conductivity after exposure to 200 ppm NO₂ changed an order of magnitude within 2-10 seconds, as shown in Figure 2.4. The conductivity was then able to be returned to normal levels with a 12 hour long pure Argon purge. Tests with 1% NH₃ caused a conductivity decrease of 1-2 orders of magnitude in 1-2 minutes. The authors concluded that these results were very promising for the use of CNT's as reusable chemical sensors.

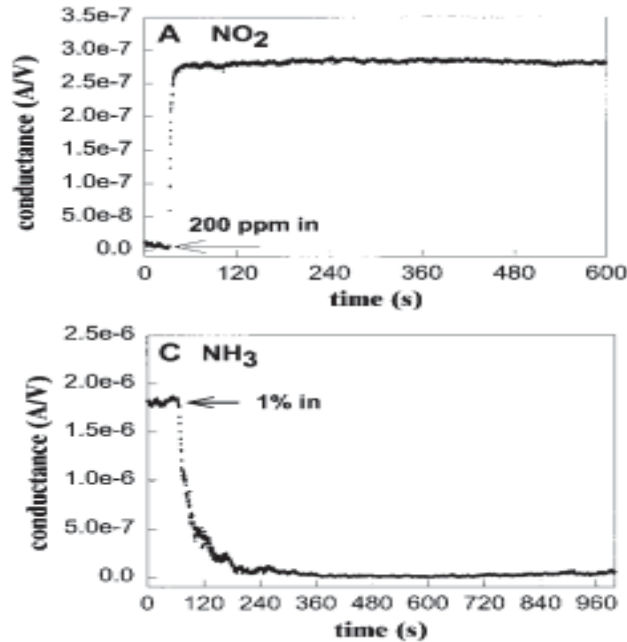


Figure 2.4. Conductance of a CNT vs time after being exposed to different gases. The conductance rapidly changes an order of magnitude when exposed to NO₂ and decreases 1-2 orders of magnitude when exposed to NH₃.

Kong et al's own density functional theory tests revealed an adsorption energy of 0.9 eV for NO₂ binding with a (10,0) SWCNT and a 0.1 electron charge transfer. However, NH₃ did not appear to bond with the CNT, which raises the question of how exactly the NH₃ affects the CNT as it does for future studies. Repeating the gas experiments on bulk CNT mats produced noticeable effects, but not nearly as large effects as on single nanotubes. This they attributed to the presence of metallic CNT's in the mats which largely dominated the conductive properties, and the inability for the gases to get to the interior tubes in the mat [19].

Avouris et al however, observed that after annealing SWCNTs with p-type semiconductor properties in a vacuum at 200 C for 10 hours, the SWCNTs demonstrated n-type semiconductor behavior [20]. Exposure to O₂ then quickly reversed these changes, causing the SWCNTs to act as p-type semiconductors once again. Thus, they showed that the p-type behavior was not an intrinsic property of the CNTs, but a result of exposure to O₂. They were

also able to use polymethyl methacrylate (PMMA) to protect the n-type properties resulting from the annealing from low O_2 exposure, as shown in figure 2.5.

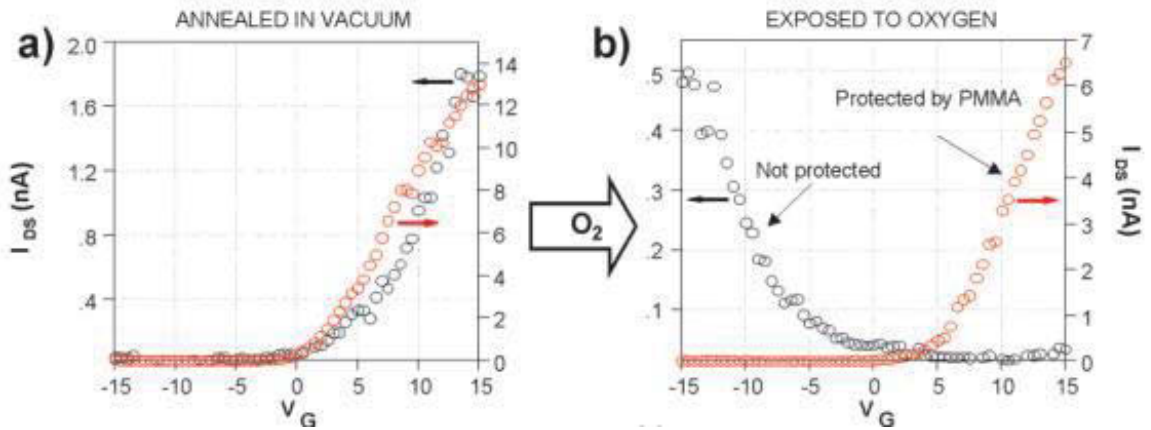


Figure 2.5. Conductivity versus gate voltage of CNTs after a) annealing and b) exposure to oxygen. The red data points represent the CNT protected by PMMA, and maintains its n-type properties, while the unprotected CNT changes to p-type upon exposure to oxygen.[20]

Modeling studies were also performed on the conductivity change of a CNT as an amino acid was adsorbed onto its surface. In Abadir et al's [21] work, a (10,0) CNT was placed in separate solutions with the amino acids isoleucine (ILE) and asparagine (ASN), and molecular dynamics simulations were run to determine how the molecules would adsorb onto the CNT surface. For modeling the conductivity, a small portion of a CNT (0.85 nm long) was considered and placed between semi-infinite aluminum contacts, and one amino acid adsorbed on the CNT surface. DFT-NEGF simulations, similar to those carried out in the present study, were then run. Though a (10,0) CNT typically expresses semiconducting properties, metallic behavior was observed from the obtained results. This was attributed to metal induced states from the contacts due to the very short length of the CNT. Regardless, changes in conductance of the CNTs were clearly observed, providing further evidence of the use of CNTs as sensors [21].

Qi et al [22] also performed experimental studies involving changes in SWCNT conductivity in the presence of NH_3 and NO_2 . However, the bridge regions of their devices consisted of multiple SWCNTs which had a polyethyleneimine coating. Qi et al [22] found that

these devices were capable of detecting NO_2 at concentrations lower than 1 ppb, while having no reaction to NH_3 , up to 1% concentration. Figure 2.6 shows the change in the conductance of their device as a function of gate voltage. A clear change from p to n type behavior is observed due to the polyethyleneimine functionalization.

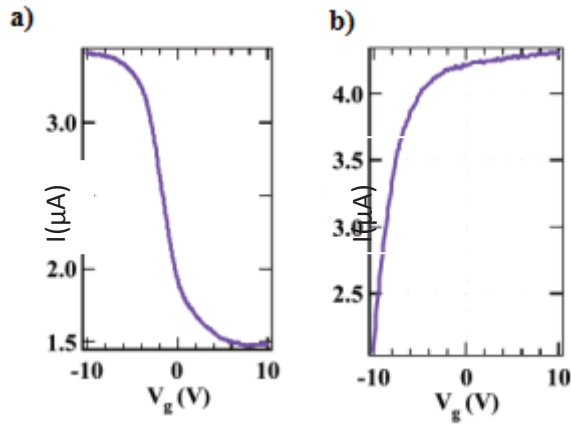


Figure 2.6. Current as a function of gate voltage for a device with untreated SWCNTs (a) and SWCNTs functionalized with polyethyleneimine (b). P type behavior is demonstrated in (a), and n type in (b). [22]

In a different use for SWCNT, Someya et al [23] investigated use of SWCNTs in a FET for detection of alcoholic vapors. By measuring changes in the threshold voltage, when the device begins to conduct at a significant level, and the maximum current, the SWCNT FET device was able to be used to detect exposure to various alcoholic vapors. Figure 2.7 shows the response of the device to a dry nitrogen stream and a saturated ethanol vapor stream. After a small spike, the current passing through the device drops to around half after being exposed to ethanol.

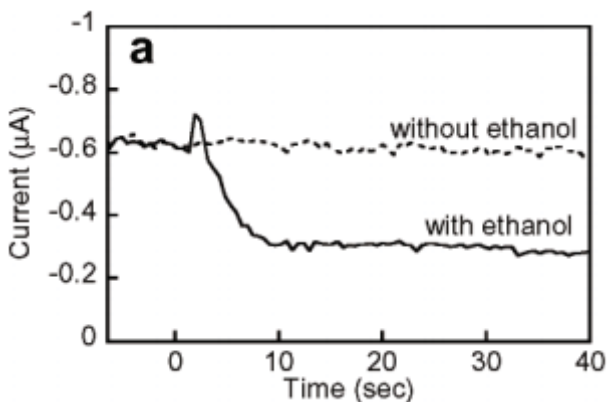


Figure 2.7 Reaction of a SWCNT FET to a stream of saturated ethanol vapor. [23]

2.3 Studies on Multiple CNT Systems

The effects of several CNTs proximity to each other has also been investigated. Gong et al [24] modeled the intrinsic and contact resistance of CNTs as a function of the distance between them using a model based on the Landauer-Büttiker formula and Monte Carlo simulation. In their study, Nanotubes that were closer than their van der Waals separation distance of 0.34 nm were subject to radial deformation, as illustrated in figure 2.8. They observed a rapid decrease in the contact resistance as CNTs approached each other. In other words, electrons were more easily able to move from one nanotube to the other as they became closer. If the nanotubes moved closer than 0.34 nm, the contact resistance would continue to slowly decrease, but the intrinsic resistance of the individual CNTs would increase at a faster rate, which matches experimental data (see figure 2.9). This increase in the intrinsic resistance is stated to be due to the increase of scattering caused by the deformation. They also examined the effects of the angle of the intersection on the total resistance of a deformed CNT junction. As expected, the minimum resistance was found to be at a 90 degree, right angle intersection, as this minimizes the deformed area. The resistance increases slowly at first as more area becomes deformed, then extremely rapidly as the tubes approach a parallel position, as shown in figure 2.10 [24].

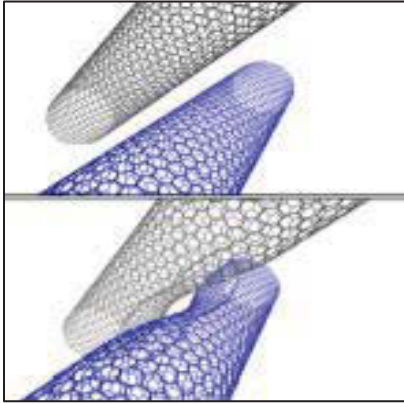


Figure 2.8. CNTs (top) become deformed as they move closer than 0.34 nm [24].

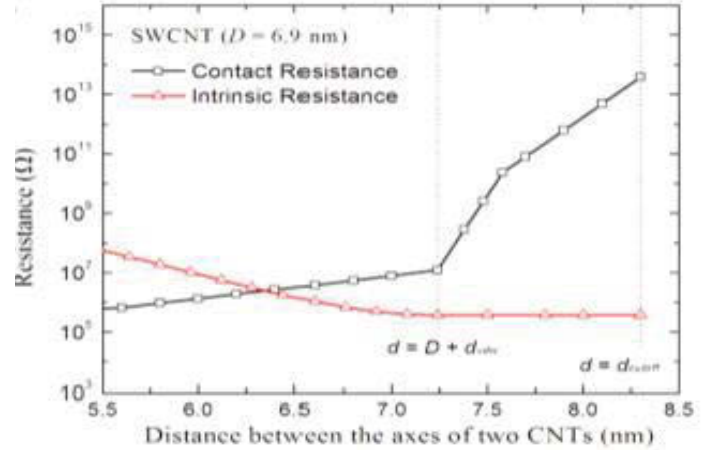


Figure 2.9. Graph of resistance vs distance between CNT axes. The intrinsic resistance stays constant until deformation begins at $d = D + d_{vdw}$ (tube diameter) + Van der Waal distance (0.34 nm) [24]

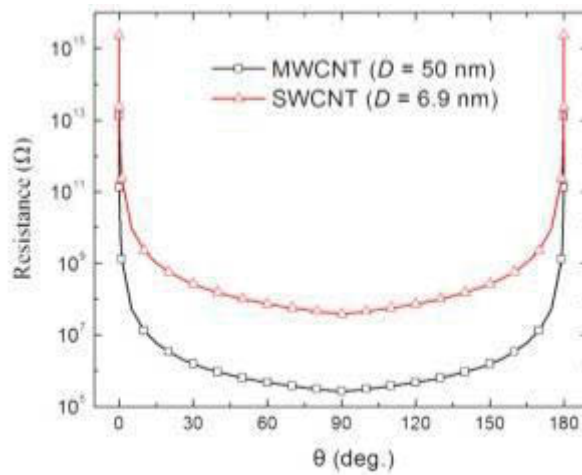


Figure 2.10. Total junction resistance of two deformed CNTs as a function of the junction angle. Resistance increases rapidly by orders of magnitude as the tubes approach a parallel orientation [24].

The properties of resistance of CNT networks were also studied by Allaouia et al [25]. In this work, a mass of randomly orientated CNTs was placed under compressive force until it reached up to 20% volume fraction CNT. As seen in figure 2.11, this led to an overall decrease of resistance in the CNT network. The researchers acknowledge the decrease in CNT contact distance as a probable explanation for this effect. It could be theorized based on the above research that if the CNTs were put under enough pressure where deformation begins to occur, the intrinsic resistance of the CNTs would begin to rise rapidly, followed by the CNTs breaking apart.

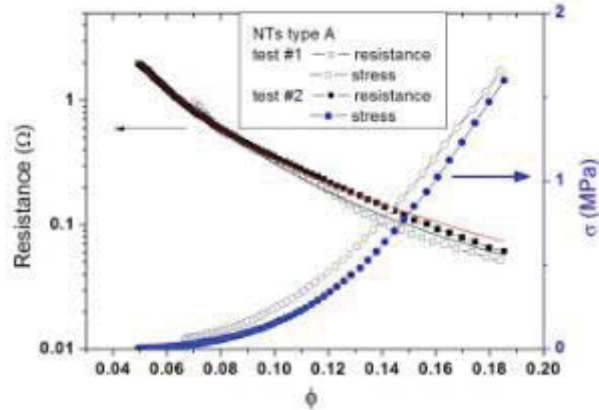


Figure 2.11. The resistance (left axis), and stress (right axis), are plotted as functions of the volume fraction of randomly orientated CNTs. The increase of compression and CNT volume fraction led to a decrease in resistance, likely due to reduced separation distance[25].

Chapter 3. Modeling

All modeling in this research work was performed using the DFTB+ modeling program on a Linux based operating system [25-32]. The following sections examine some of the theory behind the calculations performed by the program, though the sources referenced are recommended for more complete summaries of the procedures.

3.1 Density Functional Tight Binding Theory (DFTB)

Tight Binding DFT first began with the Slater and Koster 1954 paper titled "Simplified LCAO- Method for the Periodic Potential Problem". This method utilizes linear combination of atomic orbitals originally proposed by Bloch [33]. Slater and Koster sought to reduce the computational difficulty of this method, while retaining the relative accuracy of it, by fitting some of the integrals to calculations made by other methods instead of directly computing them [34]. Their method consisted of first setting up Bloch sums (as shown in equation 3.1) over each atomic orbital, and subsequently, using a linear combination of these Bloch sums to construct a wave function for a given k value ($2\pi/\lambda$, where λ is wavelength). In these sums, $\varphi_n(\mathbf{r} - \mathbf{R}_i)$ is an atomic orbital located on an atom at vector \mathbf{R}_i . In general, this results in a secular problem

(or characteristic equation problem) with an order equal to the number of atomic orbitals. The k values are then grouped into bands depending on their energy.

$$\sum(\mathbf{R}_i) \exp(i\mathbf{k} \cdot \mathbf{R}_i) \varphi_n(\mathbf{r} - \mathbf{R}_i) \quad (3.1)$$

The Slater and Koster method begins by setting up linear combinations of atomic orbitals in a way that they are orthogonal to orbitals on different atoms using Löwdin's method of symmetrical orthogonalisation [35]. These combinations of orbitals are then used to form Bloch sums. The matrix element of the energy between two Bloch sums is then expressed as:

$$\sum(\mathbf{R}_i) \exp i\mathbf{k} (\mathbf{R}_j - \mathbf{R}_i) \int \psi_n^*(\mathbf{r} - \mathbf{R}_i) H \psi_m(\mathbf{r} - \mathbf{R}_j) dv \quad (3.2)$$

where $\psi_{n,m}$ represents the Löwdin functions made through Löwdin's method, \mathbf{R}_i is the atom position that ψ_n is located on, while \mathbf{R}_j is the atom position that ψ_m is located on, with H being the hamiltonian operator.

However, this prescription leads to a three center integral which is very difficult and time consuming to calculate. To simplify this, Slater and Koster replace the integrals with constants, which they note will become smaller as the distance between the atoms that ψ are based on increases. Because of this, they assumed that beyond a certain distance, the values for the integrals will be zero. The number of integrals needed to be calculated is further reduced by symmetry arguments. Subsequently, they presented a system for defining the two-center integrals, as shown in table 3.1 [33].

$E_{s,s}$	$(ss\sigma)$
$E_{s,x}$	$l(sp\sigma)$
$E_{x,x}$	$l^2(p\rho\sigma) + (1-l^2)(p\rho\pi)$
$E_{x,y}$	$lm(p\rho\sigma) - lm(p\rho\pi)$
$E_{x,z}$	$ln(p\rho\sigma) - ln(p\rho\pi)$
$E_{x,xy}$	$\sqrt{3}lm(sd\sigma)$
E_{x,x^2-y^2}	$\frac{1}{2}\sqrt{3}(l^2-m^2)(sd\sigma)$
$E_{x,3x^2-r^2}$	$[n^2 - \frac{1}{2}(l^2+m^2)](sd\sigma)$
$E_{x,\pi y}$	$\sqrt{3}l^2m(p\rho\sigma) + m(1-2l^2)(p\rho\pi)$
$E_{x,yz}$	$\sqrt{3}lmn(p\rho\sigma) - 2lmn(p\rho\pi)$
$E_{x,zz}$	$\sqrt{3}l^2n(p\rho\sigma) + n(1-2l^2)(p\rho\pi)$
E_{x,x^2-y^2}	$\frac{1}{2}\sqrt{3}l(l^2-m^2)(p\rho\sigma) + l(1-l^2+m^2)(p\rho\pi)$
E_{y,x^2-y^2}	$\frac{1}{2}\sqrt{3}m(l^2-m^2)(p\rho\sigma) - m(1+l^2-m^2)(p\rho\pi)$
E_{x,x^2-y^2}	$\frac{1}{2}\sqrt{3}n(l^2-m^2)(p\rho\sigma) - n(l^2-m^2)(p\rho\pi)$
$E_{x,3x^2-r^2}$	$l[n^2 - \frac{1}{2}(l^2+m^2)](p\rho\sigma) - \sqrt{3}ln^2(p\rho\pi)$
$E_{y,3x^2-r^2}$	$m[n^2 - \frac{1}{2}(l^2+m^2)](p\rho\sigma) - \sqrt{3}mn^2(p\rho\pi)$
$E_{x,3x^2-r^2}$	$n[n^2 - \frac{1}{2}(l^2+m^2)](p\rho\sigma) + \sqrt{3}n(l^2+m^2)(p\rho\pi)$
$E_{xy,\pi y}$	$3l^2m^2(dd\sigma) + (l^2+m^2-4l^2m^2)(dd\pi) + (n^2+l^2m^2)(dd\delta)$
$E_{xy,yz}$	$3lm^2n(dd\sigma) + ln(1-4m^2)(dd\pi) + ln(m^2-1)(dd\delta)$
$E_{xy,zz}$	$3l^2mn(dd\sigma) + mn(1-4l^2)(dd\pi) + mn(l^2-1)(dd\delta)$
E_{xy,x^2-y^2}	$\frac{3}{2}lm(l^2-m^2)(dd\sigma) + 2lm(m^2-l^2)(dd\pi) + \frac{1}{2}lm(l^2-m^2)(dd\delta)$
E_{yx,x^2-y^2}	$\frac{3}{2}mn(l^2-m^2)(dd\sigma) - mn[1+2(l^2-m^2)](dd\pi) + mn[1+\frac{1}{2}(l^2-m^2)](dd\delta)$
E_{zx,x^2-y^2}	$\frac{3}{2}nl(l^2-m^2)(dd\sigma) + nl[1-2(l^2-m^2)](dd\pi) - nl[1-\frac{1}{2}(l^2-m^2)](dd\delta)$
$E_{xy,3x^2-r^2}$	$\sqrt{3}lm[n^2 - \frac{1}{2}(l^2+m^2)](dd\sigma) - 2\sqrt{3}lmn^2(dd\pi) + \frac{1}{2}\sqrt{3}lm(1+n^2)(dd\delta)$
$E_{yx,3x^2-r^2}$	$\sqrt{3}mn[n^2 - \frac{1}{2}(l^2+m^2)](dd\sigma) + \sqrt{3}mn(l^2+m^2-n^2)(dd\pi) - \frac{1}{2}\sqrt{3}mn(l^2+m^2)(dd\delta)$
$E_{xz,3x^2-r^2}$	$\sqrt{3}ln[n^2 - \frac{1}{2}(l^2+m^2)](dd\sigma) + \sqrt{3}ln(l^2+m^2-n^2)(dd\pi) - \frac{1}{2}\sqrt{3}ln(l^2+m^2)(dd\delta)$
$E_{x^2-y^2,x^2-y^2}$	$\frac{2}{3}(l^2-m^2)^2(dd\sigma) + [l^2+m^2 - (l^2-m^2)^2](dd\pi) + [n^2 + \frac{1}{2}(l^2-m^2)^2](dd\delta)$
$E_{x^2-y^2,3x^2-r^2}$	$\frac{1}{2}\sqrt{3}(l^2-m^2)[n^2 - \frac{1}{2}(l^2+m^2)](dd\sigma) + \sqrt{3}n^2(m^2-l^2)(dd\pi) + \frac{1}{2}\sqrt{3}(1+n^2)(l^2-m^2)(dd\delta)$
$E_{3x^2-r^2,3x^2-r^2}$	$[n^2 - \frac{1}{2}(l^2+m^2)]^2(dd\sigma) + 3n^2(l^2+m^2)(dd\pi) + \frac{2}{3}(l^2+m^2)^2(dd\delta)$

Table 3.1 Energy integrals for crystal in terms of two-center integrals.[33]

This table provides a method to split the integrals from equation 3.2 into combinations of two-center integrals. The left column indicates the integral, $E_{A,B}$, where A and B are the two orbitals being considered. For example, $E_{x,x}$ indicates an integral where the two Löwdin functions are p_x orbital-like functions. This integral can thus be expressed as a combination of two center integrals, the two p σ orbitals integral and the two p π orbitals. This is done with the goal of reducing the total number of different integrals computed by breaking down the E integrals into smaller parts which may be shared with other E integrals.

DFTB uses Kohn-Sham eigenstates, ψ_i , to represent the electron density, $n(r)$, across a space. The total energy can then be written as a function of this electron density, with the ground state electron density minimizing the total energy (see equation 3.3) [36].

$$E = \sum\{\psi_i | H^0 | \psi_i\} - \frac{1}{2} \int \int \frac{n(r)n(r')}{|r-r'|} d^3r d^3r' - \int V_{xc}[n] n(r) d^3r + E_{xc}[n(r)] + \frac{1}{2} \sum \frac{Z_\alpha Z_\beta}{|R_\alpha - R_\beta|} \quad (3.3)$$

Foulkes and Haydock explain how if $\delta n(r)$ is a small normalization-conserving fluctuation about the optimal density, then the energy equation can be written as

$$E = \sum\{\psi_i | H^0 | \psi_i\} - \frac{1}{2} \int \int \frac{n_0(r')n_0(r)}{|r-r'|} d^3r d^3r' + E_{xc}[n_0] - \int V_{xc}[n_0] n_0(r) d^3r + E_N + \frac{1}{2} \int \int \left(\frac{1}{|r-r'|} + \frac{\delta^2 E_{xc}}{\delta n \delta n'} \right) \delta n \delta n' d^3r d^3r' \quad (3.4)$$

Here the nuclear repulsion term $\left(\frac{Z_\alpha Z_\beta}{|R_\alpha - R_\beta|} \right)$ from the equation 3.3 can be represented by E_N . Equation 3.4 can be further simplified by defining a repulsive energy contribution E_{rep} as (the first order terms in δn do not appear since the fluctuations are considered to be about the optimal density $n(r)$) [36]

$$E_{rep}[n_0] = -\frac{1}{2} \int \int \frac{n_0(r')n_0(r)}{|r-r'|} d^3r d^3r' + E_{xc}[n_0] - \int V_{xc}[n_0] n_0(r) d^3r + E_N \quad (3.5)$$

It is worth noting that this equation (term) contains the electron and nuclear repulsion terms, as well as the exchange and correlation terms. Furthermore, the sixth term in equation (3.4) can be represented as E_{2nd} , and is associated to terms that are second order in δn , or density fluctuations. With these simplifications, equation 3.4 is written as

$$E = \sum\{\psi_i | H^0 | \psi_i\} + E_{rep} + E_{2nd} \quad (3.6)$$

The initial charge density is guessed as a summation of atom-like charge densities where each are neutral overall, eliminating long-range Coulomb interactions.

E_{2nd} is rewritten by breaking the density fluctuations, δn , into atom centered contributions δn_α and δn_β , similar to what is carried out with the charge density. These contributions can then be broken into radial functions as shown in equation (3.7)

$$\delta n_\alpha(r) = \sum_{lm} K_{ml} F_{ml}^\alpha (|r - R_\alpha|) Y_{lm} \left(\frac{r - R_\alpha}{|r - R_\alpha|} \right) \approx \Delta q_\alpha F_{00}^\alpha (|r - R_\alpha|) Y_{00} \quad (3.7)$$

This leads to E_{2nd} being represented as

$$E_{2nd} = \frac{1}{2} \sum_{\alpha\beta}^N \Delta q_\alpha \Delta q_\beta \gamma_{\alpha\beta}, \quad (3.8)$$

where

$$\gamma_{\alpha\beta} = \iint' \Gamma[r, r', n_0] \frac{F_{00}^\alpha (|r - R_\alpha|) F_{00}^\beta (|r' - R_\beta|)}{4\pi} \quad (3.9)$$

From this point, $\gamma_{\alpha\alpha}$ is approximated by the difference of the atomic ionisation potential and electron affinity [37]. This difference is related to the Hubbard parameter U_α , which can be calculated for an atom in DFT as the second derivative of the total energy of the atom with respect to its atomic charge. This is under the monopole approximation, which restricts δn to being like a 1s orbital. Here the influence of the environment on intra-atomic electron interaction is also neglected. This derivative is then expressed as the derivative of the energy of the highest occupied atomic orbital with respect to its occupation number [36, 38, 39]. Thus, if $\gamma_{\alpha\alpha} = U_\alpha$, $\gamma_{\alpha\beta}$ can be found by using equation 3.9 and 3.10 [39].

$$F_{00}^\alpha = \frac{\tau_\alpha}{8\pi} \exp(-\tau_\alpha |r - R_\alpha|), \quad \tau_\alpha = \frac{16}{5} \gamma_{\alpha\alpha} \quad (3.10)$$

Thus, the tight binding form of the total energy equation 3.4 can be expressed as

$$E = \sum \{\psi_i | H^0 | \psi_i\} + \frac{1}{2} \sum \gamma_{\alpha\beta} \Delta q_\alpha \Delta q_\beta + E_{rep} \quad (3.11)$$

The Kohn-Sham wave functions are expanded into localized atomic orbitals, where pseudopotential contributions are ignored and only the potential contributions from two center

matrix elements are included. This leads to the matrix elements of the ground state of the hamiltonian, $H_{\mu\nu}^0$ being expressed as

$$H_{\mu\nu}^0 = \begin{cases} \epsilon_{\mu}^{\text{free atom}}, & \mu = \nu \\ \langle \phi_{\mu} | \hat{T} + v_{\text{eff}}[n_{\alpha}^0 + n_{\beta}^0] | \phi_{\nu} \rangle, & \mu \in \alpha, \nu \in \beta. \end{cases} \quad (3.12)$$

Basis functions ϕ_{ν} are then written as psuedo atomic wave functions in terms of Slater orbitals and spherical harmonics. The basis functions and input densities n^0 are defined by a Schroedinger equation as shown in equation (3.13). See [40] for charts with values of the hamiltonian matrices and overlap matrices for carbon-hydrogen interactions.

$$[\hat{T} + v_{\text{eff}}[n_{\alpha}^0] + \left(\frac{r}{1.85r_{\text{cov}}}\right)^2] \varphi_{\nu}(\mathbf{r}) = \epsilon_{\nu} \varphi_{\nu}(\mathbf{r}) \quad (3.13)$$

where

$$v_{\text{eff}}[n_0] = V_{\text{ext}} + \int' \frac{n_0'}{|r-r'|} + V_{\text{xc}}[n_0]$$

Here, V_{xc} is calculated using the local-density approximation as parameterized by Perdew and Zunger (41); and the one electron potential is treated as the sum of spherical atomic Kohn-Sham potentials of a neutral pseudoatom from its compressed electron density [40].

3.2 Non-Equilibrium Green's Functions

The Green's Function formalism is utilized for determining the current flow by working at the molecular level. Non-Equilibrium Green's Functions take advantage of the fact that that the contacts are very large compared to the molecular bridge to divide the system into three regions. The system components are the main center device region consisting of the molecular bridge between the contacts, and the regions of the contacts that are affected by the molecule. The treatment of the contact regions is based on bulk properties, which do not differ from the

presence of the molecule, and the effects of the contact are included in calculations as a self energy, Σ_α [42].

The NEGF transport calculations are performed by first dividing up the system into 3 sections; a source contact, a drain contact, and the middle device region. These layers are further broken up into principal layers, with each layer only having interactions with the adjacent layers. The contacts are treated as semi-infinite sections, possessing their bulk properties. Fixing the potentials of the contacts at different values causes electron flow across the device region. The whole total potential drop is thus assumed to occur over this device region, since the contacts are taken to be equipotential regions. The charge density matrix in NEGF is defined as [13]

$$\rho = \frac{1}{2\pi i} \int_{-\infty}^{+\infty} dE G^<(E) \quad (3.14)$$

Here, $G^<$ represents the electron-electron correlation matrix. This can be expressed as

$$\rho = \int_{-\infty}^{+\infty} dE f_c(E) G^r(E) - \int_{-\infty}^{+\infty} dE f_c(E) G^a(E) + \sum_{\alpha \neq c} dE [f_\alpha(E) - f_c(E)] G^r(E) \Gamma_\alpha(E) G^a(E) \quad (3.15)$$

$$\text{where } \Gamma_\alpha(E) = i[\Sigma_\alpha^r(E) - \Sigma_\alpha^{r\dagger}(E)] \quad (3.16)$$

In equation 3.15, f_c is a fermi function related to the contact at the lower potential (the collector contact). Γ_α is known as the broadening function, and is related to the broadened density of states in the bridge or channel region. The first two integrals are evaluated using contour integration in the complex plane while the final sum is on the real axis. The contact self energies, Σ_α , are computed as

$$\Sigma_\alpha = T_{L(\alpha),\alpha} g_{\alpha,\alpha} T_{\alpha,L(\alpha)} \quad (3.17)$$

$$T_{L,L+1} = ES_{L,L+1} - H_{L,L+1} \quad (3.18)$$

where $L(\alpha)$ refers to the device layer that interacts with the contact, and g is the surface green's function. The surface green's function for layer L , interacting only with the right part of the system, is represented as.

$$g_{L,L}^R = [ES_{L,L} - H_{L,L} - T_{L,L+1} g_{L+1,L+1}^R T_{L+1,L}]^{-1} \quad (3.19)$$

where $S_{L,L}$ and $H_{L,L}$ represent overlap and hamiltonian matrices of the given layers. The green's functions are then solved by iteration, starting from the left side of the region by using Equations 3.20 – 3.24 [13].

$$G_{1,1} = [ES_{1,1} - H_{1,1} - \Sigma_{1,1} - T_{1,2} g_{2,2}^R T_{2,1}]^{-1} \quad (3.20)$$

$$G_{L,L} = g_{L,L}^R + g_{L,L}^R T_{L,L-1} G_{L-1,L-1} T_{L-1,L} g_{L,L}^R \quad (3.21)$$

$$G_{L-1,L} = -G_{L-1,L-1} T_{L-1,L} g_{L,L}^R \quad (3.22)$$

$$G_{L,L-1} = -g_{L,L}^R T_{L,L-1} G_{L-1,L-1} \quad (3.23)$$

$$G_{L,L}^{<,\alpha} = G_{L,L(\alpha)}^R \Gamma_\alpha G_{L,L(\alpha)}^{R\dagger} \quad (3.24)$$

3.3 Poisson Solver

Using the electron density found by the NEGF computations, the Hartree potential is computed by the Poisson equation. First, the total electronic density is expressed as a combination of neutral atoms and density fluctuations [13].

$$n(r) = \sum_i [n_i^0(r) + F_{00}^i(r) \Delta q_i] \quad (3.25)$$

Here n_i^0 represents the neutral atomic densities, F_{00}^i are the radial functions and Δq_i are the Mulliken charges. The Poisson equation for mean-field electrostatic potential is given by:

$$\nabla^2 V = 4\pi \sum_i [n_i^0(r) + F_{00}^i(r) \Delta q_i] + \text{Boundary conditions} \quad (3.26)$$

The boundary conditions for this problem are implemented by insisting that the potential in the contacts must be equal to that of the corresponding bulk medium, shifted by any potential bias of the contact.

In Pecchia et al's [13] method, the Poisson equation is solved in three dimensional space as a general linear, non-seperable, elliptical partial equation, as shown below

$$\sum_{t=x,y,z} c_u(\mathbf{r}) \delta_t^2 V(\mathbf{r}) + \sum_{t=x,y,z} c_t(\mathbf{r}) \delta_t V(\mathbf{r}) + c(\mathbf{r}) V(\mathbf{r}) = \rho(\mathbf{r}) \quad (3.27)$$

with $c_t = c = 0$ and $c_u = -1/4 \pi$ for a two contact system, though other coefficients can be used for gated systems [13].

The new Hartree potential calculated here is used within the NEGF calculations to obtain the electron density. This process continues iteratively until convergence is reached. The transmission probability, $T(E)$, can then be calculated as shown in equation 3.28, and the current, through the Landauer-Buttiker formula (equation 3.29) [43].

$$T(E) = Tr[\Gamma_S G^r \Gamma_D G^a] \quad (3.28)$$

$$I = \frac{4e}{h} \int T(E) [f_S(E) - f_D(E)] dE \quad (3.29)$$

Where Tr is the matrix trace operation, and f_S and f_D represent the fermi functions of the source and drain respectively, which represents the probability that a given electron energy state will be occupied.

3.4 Single-Walled Carbon Nanotube (SWCNT) Generation and Visualizing

For the modeling performed in this work, an (8,0) zigzag SWCNT was constructed using the TubeGen Online program [44]. Default carbon-carbon bond lengths of 1.4210 angstroms and a unit cell gutter of 1.6735 Angstroms in the x or y directions for cases involving multiple cells were used, which determined the spacing between CNTs (see figure 3.1). For visualization of the SWCNTs and molecules, the program Avogadro was used [45]. The Avogadro program ensures that the atom coordinates were approximately correct, to create images for use in this work, and to perform geometry optimizations through energy minimization. Transport through the

tubes was in the z direction, which is the direction that the SWCNTs axis lay on. Here, a CNT with a length of 4 unit cells per contact and 5 unit cells for the main device region was considered.

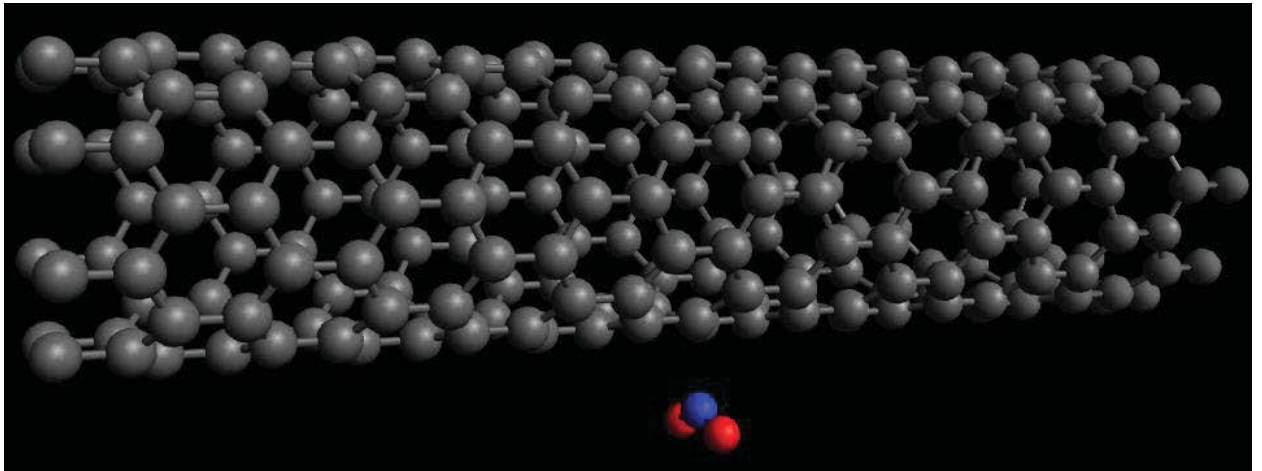


Figure 3.1. A visualization of an (8,0) SWCNT with an NO₂ molecule approximately 2.18 Å from the nanotube surface [45].

Chapter 4. Modeling Methodology

4.1 Computer Set-Up

The modeling program used in this work was based on a Linux platform, and therefore a Linux operating system was set up for this research program. Oracle VM VirtualBox (see fig. 4.1) was used to create a virtual machine with an Ubuntu Linux installation on it for modeling purposes. This allowed for modeling work to be completed while windows based word processors and spreadsheets were used for data collection and organization.

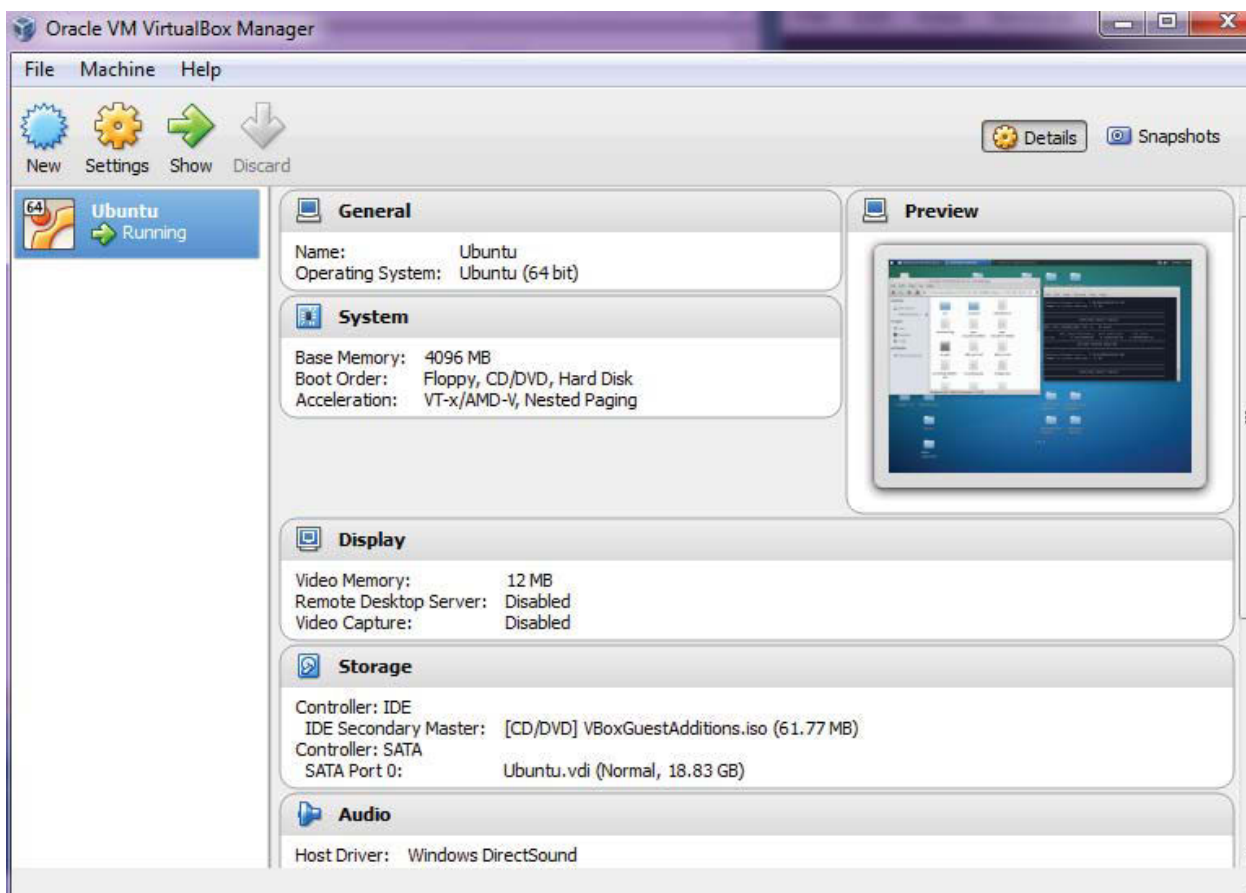


Figure 4.1 VirtualBox software used to create a virtual machine for running a Linux operating system.

The DFTB+NEGF program was then placed on the system by downloading the precompiled binary from the DFTB website [46]. It was then placed in the path folder, so the program could be executed using a simple "dftb+" command in a command prompt window.

One default path directory on this system was the "bin" folder accessed through the main file system (see fig 4.2).

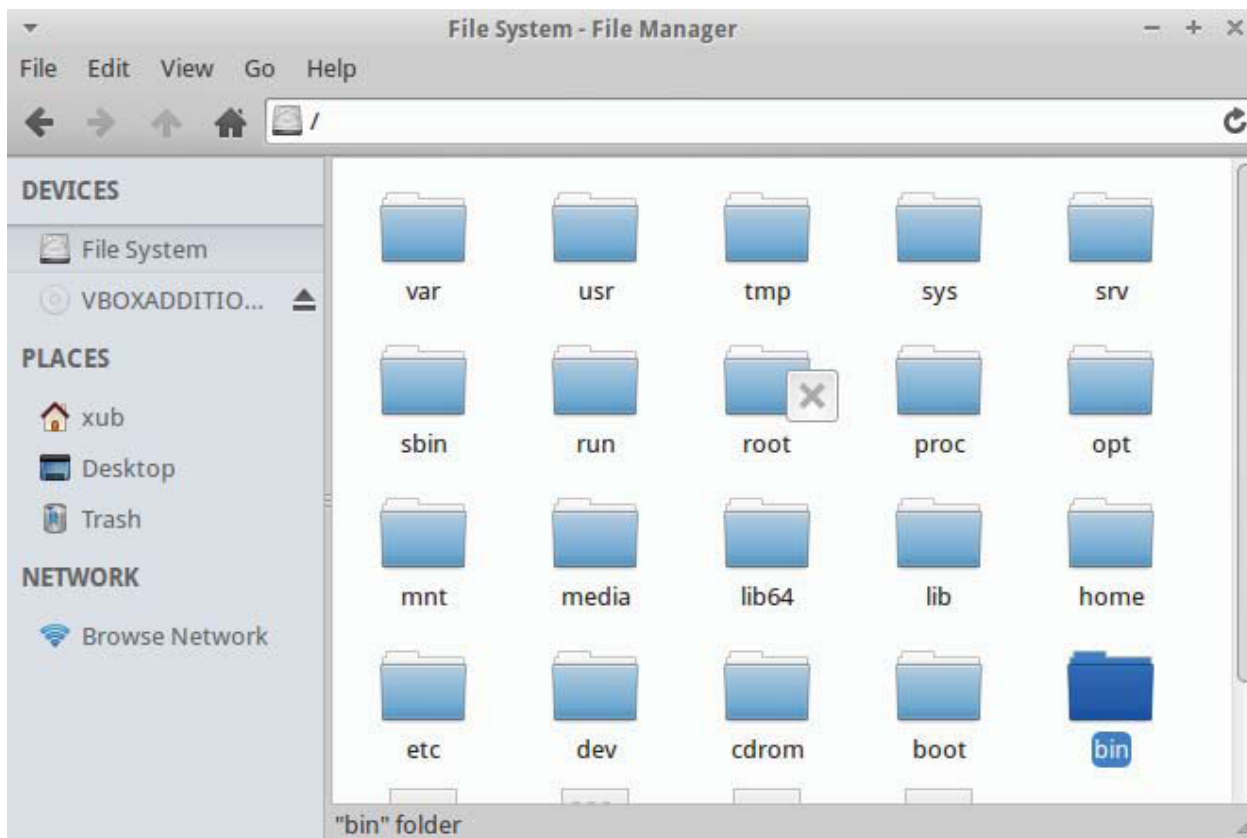


Figure 4.2 The structure of the "bin" folder where the dftb+ program was placed to allow it to be more easily executed.

4.2 Modeling Set-Up

For setting up a simulation, a folder was created on the desktop for convenience (although it can be created at any location). Inside this folder, the Slater Koster files must be placed for every interacting atom type in the system to be modeled. Several sets of these files are available on the DFTB website [47]. For example, simulations for bare SWCNTs require only a file for C-C interactions. A CNT with NO₂ molecules however, requires C-C, C-N, C-O, N-C, N-N, N-O, O-C, O-N, and O-O files, for a total of 9 Slater Koster files (see fig 4.3).

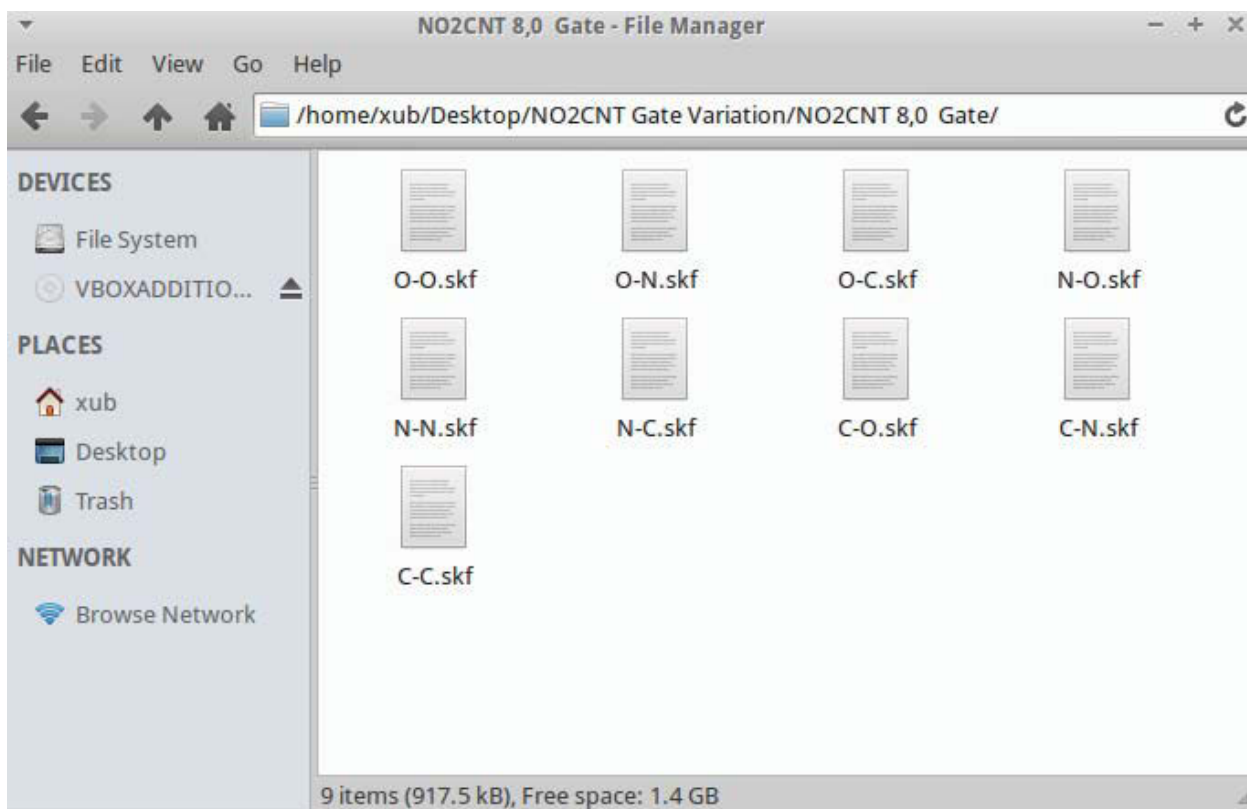


Figure 4.3. The necessary SKF files for an NO₂ doped CNT calculation.

After this, for transport calculations to be performed here, two folders must be created within this folder, these being the titled contacts, and the GS (for Ground State information) (see fig 4.4). These are left empty, and used during calculations.

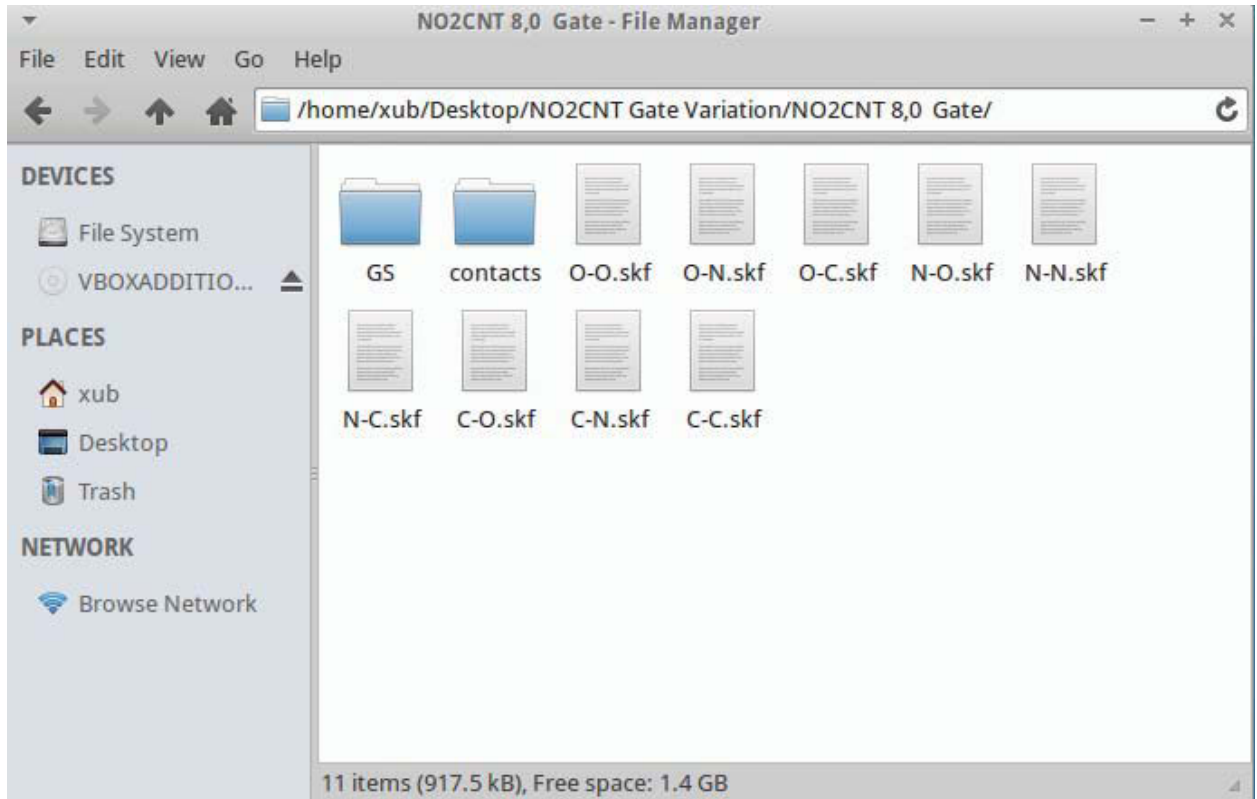


Figure 4.4. The "GS" and "contacts" folders necessary for any transport calculation

Finally, the input files for the source, drain, and device regions are added. If the geometry of the system is referred to as a separate file instead of being in the input files, that file also needs to be present (see fig 4.5).

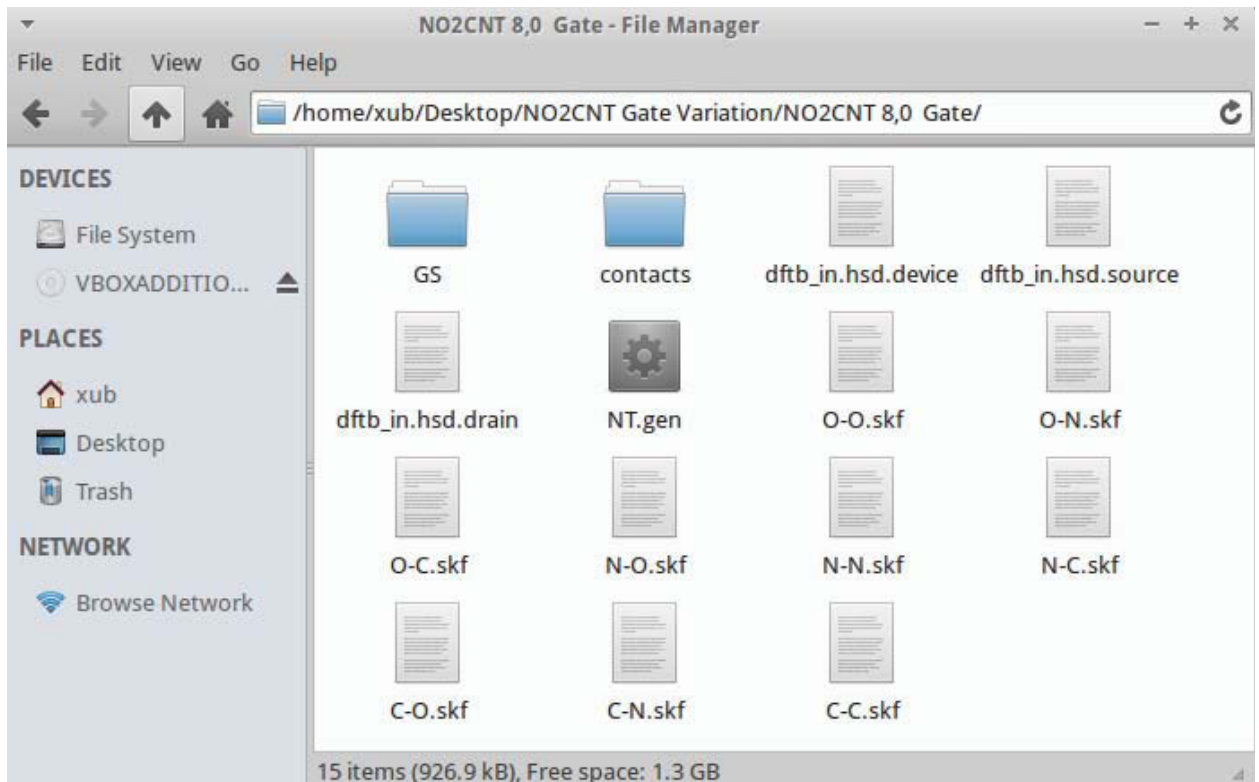


Figure 4.5. Completed folder for a gated NO₂ doped CNT.

To perform a NEGF calculation, first a DFTB calculation must be performed on the contacts to determine their bulk properties. The source input file "dftb_in.hsd.source" is renamed to "dftb_in.hsd", as this is the filename DFTB+ searches for input. Subsequently, a terminal is opened in the working folder (see fig 4.6, 4.7). To perform the DFTB contact calculation, the command "dftb+" is issued by entering it into the terminal window and pressing enter. This should result in the relatively quick calculation shown in figure 4.8.

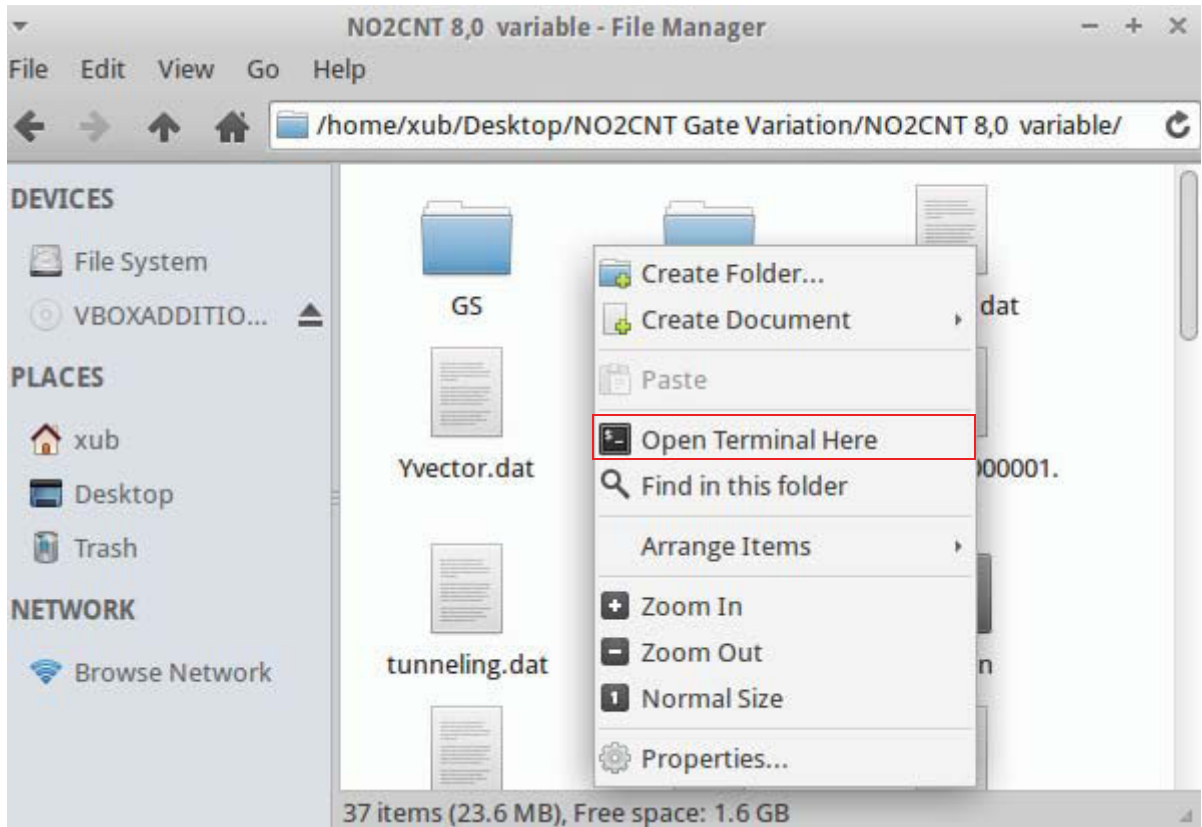


Figure 4.6. A terminal may be opened by right clicking in the folder and selecting "Open Terminal Here".

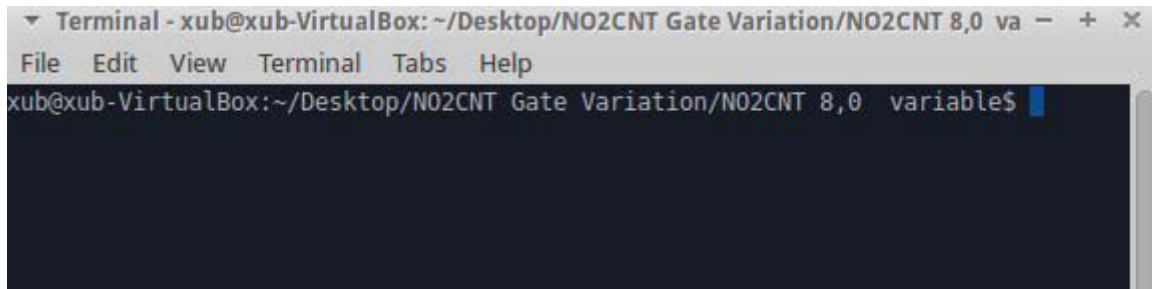


Figure 4.7 Opened Terminal window, where the "dftb+" command has to be issued.

```

Terminal - xub@xub-VirtualBox: ~/Desktop/NO2CNT Gate Variation/NO2CNT 8,0 G: - + x
File Edit View Terminal Tabs Help
      8: 0.280000 0.000000 0.000000 0.080000
      9: 0.320000 0.000000 0.000000 0.080000
     10: 0.360000 0.000000 0.000000 0.080000
     11: 0.400000 0.000000 0.000000 0.080000
     12: 0.440000 0.000000 0.000000 0.080000
     13: 0.480000 0.000000 0.000000 0.080000

Extra options:
-----
*****
** Geometry step: 0
*****

      iSCC Total electronic   Diff electronic   SCC error
scfsum:  1  -0.11546143E+03   0.00000000E+00   0.32503693E-05
scfsum:  2  -0.11546143E+03  -0.71764816E-11   0.19615614E-05
scfsum:  3  -0.11546143E+03  -0.38937742E-11   0.54516197E-07
>> Charges saved for restart in charges.bin

Total Energy:                -110.560446
Total Mermin free energy:     -110.560446
All done. Good bye!
xub@xub-VirtualBox:~/Desktop/NO2CNT Gate Variation/NO2CNT 8,0 Gate$

```

Figure 4.8 Terminal window containing a completed contact calculation resulting from dftb+ command issued in figure 4.7

If a "permission denied" occurs instead, due to file ownership and privileges, the command "sudo dftb+" may need to be issued instead of just "dftb+". After issuing this, the password of the profile created during Xubuntu installation will need to be entered (note, password entry will not echo, (ie show stars, dots, or any characters during or after being typed)).

After the contact calculation has completed, the folder will now contain a file titled "detailed.out" (see fig 4.9). In this file (see fig 4.10), one key value is the calculated fermi energy of the contact. This value should be copied and transferred into the fermi level section in the device input file, dftb_in.hsd.device (as it will be shown in section 4.4.1). The source input file must then be renamed back to the original "dftb_in.hsd.source". This process is then repeated using the drain input, "dftb_in.hsd.drain". In summary, the "dftb_in.hsd.drain" file is renamed to

"dftb_in.hsd", the "dftb+" command is issued, and the fermi level copied from the "detailed.out" file to the "dftb_in.hsd.device" file. In addition to the detailed.out file, these calculations also produce the shiftcont_drain.dat and shiftcont_source.dat files which contain additional information about the contacts for further calculations. Note these steps do not need to be repeated for gate or bias voltage changes.

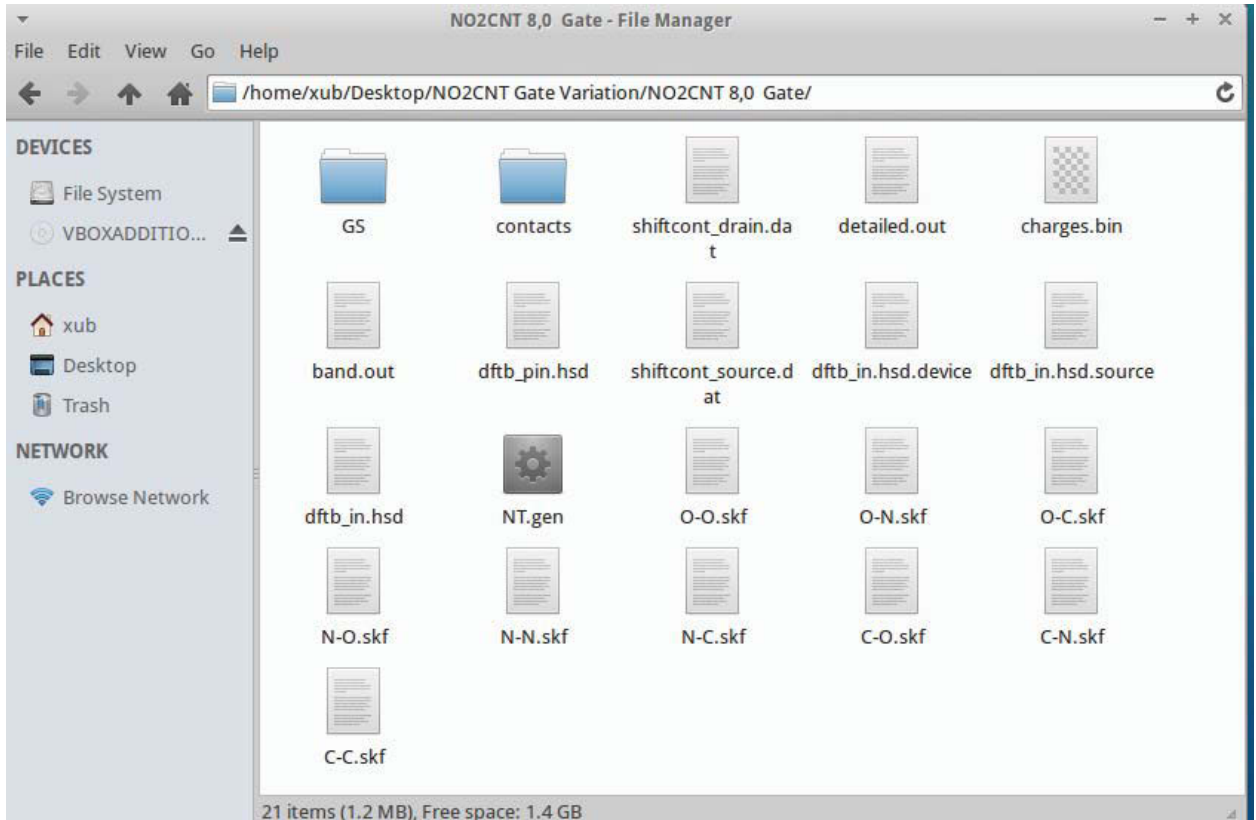


Figure 4.9. Calculation folder after contact calculation.


```

detailed.out - Mousepad
File Edit View Text Document Navigation Help
03 2 1 -1 0.92174544
63 2 1 0 0.91201223
63 2 1 1 0.98933231
64 1 0 0 1.17690981
64 2 1 -1 0.92174544
64 2 1 0 0.91201223
64 2 1 1 0.98933231

Fermi energy: -0.1414397217 H -3.848771 eV
Band energy: -115.4614319707 H -3141.865420 eV
TS: 0.0000000000 H 0.000000 eV
Band free energy (E-TS): -115.4614319707 H -3141.865420 eV
Extrapolated E(0K): -115.4614319707 H -3141.865420 eV

Input/Output charge (spin: 1): 256.00000000 256.00000000

Energy H0: -115.4614319705 H -3141.865420 eV
Energy SCC: 0.0000000000 H 0.000000 eV
Total Electronic energy: -115.4614319705 H -3141.865420 eV
Repulsive energy: 4.9009856008 H 133.362604 eV
Total energy: -110.5604463697 H -3008.502817 eV
Total Mermin free energy: -110.5604463697 H -3008.502817 eV

Calculation with static geometry

SCC converged

Filetype: None Line: 1 Column: 0 OVR

```

Figure 4.10. Output file "detailed.out" for source contact calculation

After completing these steps, the device input file "dftb.in.hsd.device" is named "dftb_in.hsd", a console opened, and the dftb+ command is run again, resulting in figures 4.11 and 4.12.

```
Terminal - xub@xub-VirtualBox: ~/Desktop/NO2CNT Gate Variation/NO2CNT 8,0 Gi - + X
File Edit View Terminal Tabs Help
=====
COMPUTING DENSITY MATRIX
=====
REAL AXIS INTEGRATION: CPU 0, 9 point
*****
iSCC Total electronic Diff electronic SCC error
scfsum: 103 -0.19304853E+03 0.11585311E-06 0.18392972E-06
=====
SOLVING POISSON EQUATION
=====
Relative Poisson Error = 1.238928257954258E-010
Number of cycles executed = 1/ 60
-----
*****
COMPUTING DENSITY MATRIX
=====
REAL AXIS INTEGRATION: CPU 0, 9 point
*****
iSCC Total electronic Diff electronic SCC error
scfsum: 104 -0.19304853E+03 0.47316860E-07 0.92092227E-07
=====
```

Figure 4.11. DFTB + NEGF calculation proceeding, alternating between computing density matrix and Poisson equation. (Image taken from nearly finished calculation)

```
Terminal - xub@xub-VirtualBox: ~/Desktop/NO2CNT Gate Variation/NO2CNT 8,0 Gi - + x
File Edit View Terminal Tabs Help
=====
COMPUTING DENSITY MATRIX
=====
REAL AXIS INTEGRATION: CPU 0, 9 point
*****
          iSCC Total electronic   Diff electronic   SCC error
scfsum: 107  -0.19304853E+03  -0.15464877E-07  0.53315050E-08
>> Charges saved for restart in charges.bin

Total Energy:                -176.196698
Total Mermin free energy:     -176.196698

=====
COMPUTING TUNNELING AND DOS
=====

Release Poisson Memory:
  peak memory allocated:    69.75 Mb
  current memory allocated:  0.00 bt
Release Negf Memory:
  peak memory allocated:    55.99 Mb
  current memory allocated:  0.00 bt
All done. Good bye!
xub@xub-VirtualBox:~/Desktop/NO2CNT Gate Variation/NO2CNT 8,0 Gate$
```

Figure 4.12 DFTB+NEGF calculation completed

The device calculation will take much longer, but again will result in a "detailed.out" file being created (replacing any one already present). The current calculated is located at the end of this file, as shown in figure 4.13.

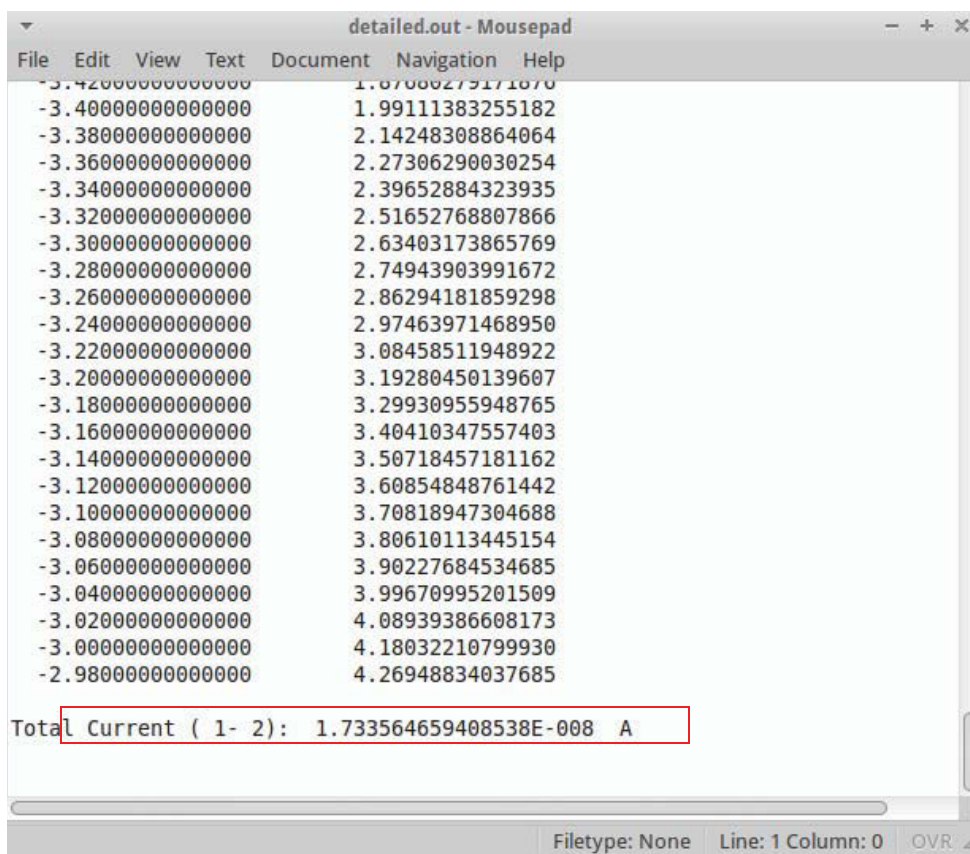


Figure 4.13. The "detailed.out" file from DFTB+NEGF calculation using the device input file.

4.3 Contact Sample Input

In this section, an input file for the source contact region of an 8,0 CNT with an NO₂ molecule 2.18 Å from the surface is presented. The following commands make up the source (dftb_in.hsd.source) and drain (dftb_in.hsd.drain) input files.

4.3.1 Geometry

This section refers to the file which contains the coordinates of the atoms of the system. While the coordinates can be entered in the file, they can also be entered in a separate file, which tends to keep the input file smaller and cleaner.

```
Geometry = GenFormat{
  <<< 'NT.gen'
}
```

In this case, a file named "NT.gen" has been created and placed in the simulation folder for establishing the coordinates of the atoms. A sample of the information in this file is shown below.

```

227 C
C N O
1 1 3.14889 -0 -4.984
2 1 3.14889 -0 -6.405
3 1 2.90919 1.20503 -2.849

```

The top row here indicates the total number of atoms in the system, which is treated as a cluster. The second row indicates types of atoms present. The bottom three rows indicate atom types and positions. The columns represent, from left to right, atom number, atom type (relative to order in 2nd row), followed by x, y, and z coordinates given in Angstroms. In the full coordinate list in "NT.gen" file, the center device region atoms are listed first. These are followed by the source atoms, and finally the drain atoms. The source and drain sections contain two principal layers, which each contain several unit cells of the contact. These layers are put with the layer closest to the device region first. The layers in each cell are identical, but shifted in the direction of current flow. So if the layers were to be called, from left to right, source layer 1, source layer 2, device, drain layer 1, and drain layer 2, then the order the atoms would be listed in the geometry file "NT.gen" would be: device, source layer 2, source layer 1, drain layer 1, drain layer 2.

In what follows, the zones of the system are defined, breaking it into the device, source, and drain regions. The AtomRange setting defines which atoms are contained in each section. Note that as stated earlier, the first atoms constitute the device region, followed by the source and drain regions. The "Task = ContactHamiltonian" expands the treatment with the inclusion of a contact calculation, either on the source or drain. Note that for the drain input file, the ContactID value here is set as "drain". In these calculations, the latter setting is the only difference between the source and drain input files.

```

Transport {
  Geometry {
    Device {
      AtomRange = 1 99
    }
    Contact {
      Id = "source"
      AtomRange = 100 163
    }
    Contact {
      Id = "drain"
      AtomRange = 164 227
    }
  }
  Task = ContactHamiltonian{
    ContactId = "source"
  }
}

```

4.3.2 Driver and Hamiltonian

This section contains the Driver and Hamiltonian settings. The Driver section contains the settings for molecular dynamics runs, which focus on the movement of molecules from various forces acting upon them. All molecules were fixed during the calculations described in this work, so the driver settings were not used, and therefore this section was consequently left empty. The Hamiltonian section sets several parameters needed to set up the Hamiltonian of the system. The MaxSCCIterations defines the maximum number of iterations that will be attempted if the SCCTolerance is not reached. More iterations are often needed for larger systems or large potential difference, though convergence was achieved for all data reported in this work. The MaxAngularMomentum sets the most distant electron shell that is included in calculations for each element. Here the "p" shells were included.

```
Driver = {}

Hamiltonian = DFTB {
  SCC = Yes
  MaxSCCIterations = 20
  SCCTolerance = 1e-8
  MaxAngularMomentum = {
    C = "p"
    N = "p"
    O = "p"
  }
}
```

4.3.3 Remaining Simulation Settings

This final section implements the Filling option, which assigns electrons to energy states following a fermi distribution, with T being the electron temperature. The SlaterKosterFiles option specifies the files that describe the interactions between the specified atoms, with a file needed for each possible interaction. The K-point sampling is set next. The values listed are ideal for 1 D wire contacts, with a large number of points along the transport direction [45], and one in the others. The Eigensolver setting then sets which solver will be used for computing eigenvalue problems during calculation.

```

Filling = Fermi {
  Temperature [Kelvin] = 0
}
SlaterKosterFiles = {
  C-C = "C-C.skf"
  C-N = "C-N.skf"
  N-C = "N-C.skf"
  C-O = "C-O.skf"
  O-C = "O-C.skf"
  N-O = "N-O.skf"
  O-N = "O-N.skf"
  N-N = "N-N.skf"
  O-O = "O-O.skf"
}

KpointsAndWeights = SupercellFolding{
  25 0 0
  0 1 0
  0 0 1
  0.0 0.0 0.0
}
Eigensolver = DivideAndConquer{}
}

```

4. 4 Device Sample Input

In this section, the input file for the device region of an 8,0 CNT with an NO₂ molecule 2.18 Å from the surface is presented. Sections differing from those of the above source/drain input file will be examined and explained. These settings would make up the "dftb_in.hsd.device" file.

4. 4.1 Geometry and Initial Settings

The Geometry and Transport sections here are the same as in the transport calculations in section 4.3.1. The UploadContacts line in this section obtains the information from the DFTB calculations of the contacts performed prior to the device region calculation. FermiLevel sets the fermi level of the contacts. This value was obtained in the "detailed.out" file from the contact calculations (see figure 4.10). If the base fermi levels of the source and drain contact differ, due

to them being different materials, then the fermi levels must be set for each, similar to the contact potentials. In this case, as the contacts are identical, their initial Fermi level was the same for each, and the "SetForAll" option was therefore used. The ContactPotentials sets the potentials of each contact, which leads to a shift in its Fermi level. EnergyRange sets the range that the transmission and state density are calculated over, which should be centered around the Fermi level of the contacts, covering the bands through which transport may occur. EnergyStep determines how many points in the energy range are examined by setting the difference between points, or the step size.

```
Geometry = GenFormat{
<<< 'NT.gen'
}

Transport {
  Geometry {
    Device {
      AtomRange = 1 99
    }
    Contact {
      Id = "source"
      AtomRange = 100 163
    }
    Contact {
      Id = "drain"
      AtomRange = 164 227
    }
  }
}

Task = UploadContacts {
  FirstLayerAtoms = 1
  FermiLevel [eV] = SetForAll {-3.848771}
  ContactPotentials {
    source [ev]= 0.0
    drain [eV] = 1.5
  }
  EnergyRange [eV] = -6 -3
  EnergyStep [eV] = 0.020
  WriteTunneling = Yes
}
```

```
}
```

4.4.2 Driver and Hamiltonian

This section contains the Driver and Hamiltonian settings. These are the same as in the source calculation shown in section 4.3.2. To speed convergence and help prevent oscillations, charges from the previous calculation iterations are mixed together, and the mixer configures the system used to calculate this charge mixing. If a calculation has difficulties converging, lowering the `MixingParameter` setting from the default 0.20 can often help.

```
Driver = {}  
  
Hamiltonian = DFTB {  
  SCC = Yes  
  MaxSCCIterations = 200  
  SCCTolerance = 1e-8  
  Mixer=Broyden{MixingParameter=0.02}  
  MaxAngularMomentum = {  
    C = "p"  
    N = "p"  
    O = "p"  
  }  
}
```

4.3.3 Poisson Solver

Section 3 configures the Poisson solver used for the NEGF equations. `Poissonbox` determines the length of the Poisson box in each spatial dimension. `MinimalGrid` specifies the minimal, coarsest grid spacing for the Poisson box in each dimension, though the actual spacing is set to less than these internally. Here, lower settings will increase accuracy, but increase computational time. `AtomDensityTolerance` determines the cutoff at which a charge is set to be zero.

```

Filling = Fermi {
}
SlaterKosterFiles = {
  C-C = "C-C.skf"
  C-N = "C-N.skf"
  N-C = "N-C.skf"
  C-O = "C-O.skf"
  O-C = "O-C.skf"
  N-O = "N-O.skf"
  O-N = "O-N.skf"
  N-N = "N-N.skf"
  O-O = "O-O.skf"
}
Electrostatics = Poisson {
Poissonbox [Angstrom] = 20.0 30.0 20.0
  MinimalGrid [Angstrom] = 0.4 0.4 0.4
  BuildBulkPotential = Yes
  SavePotential = Yes
  AtomDensityTolerance = 1e-5
  PoissonAccuracy = 1e-6
}

```

4.3.4 Gate Settings

This section specifies the settings for a planar gate in the system. The `GateLength_l` specifies the length in the transport direction (z), while `GateLength_t`, specifies it in the x direction. `GateDistance` is the distance (in y) from the center axis. In this run, the gate potential was a parameter determined as a function of the sensing capabilities.

```

Gate = Planar {
  GateLength_l [Angstrom] = 7.0
  GateLength_t [Angstrom] = 30.0

  GateDistance [Angstrom] = 7.0
  GatePotential [eV] = -7
}

```

4.3.5 Green's Function's Solver

This section configures the Green's Functions solver. `Delta` is simply a small positive number. `LowestEnergy`, `ContourPoints`, and `EnclosedPoles` all relate to the contour integration used for the Green's Functions. Increasing the number of contour points will lead to increased

calculation times, but may help if a simulation is experiencing convergence issues. Lowest energy specifies the starting point of integration, while enclosed poles is only relevant for finite temperature calculations, and is usually set at 3 to 5.

```
Eigsolver = GreensFunction {  
  FirstLayerAtoms = 1  
  Delta [eV] = 1e-5  
  ContourPoints = 30 40  
  LowestEnergy [eV] = -60.0  
  EnclosedPoles = 4  
}
```

Chapter 5. Results and Discussion

This chapter examines the results of the modeling work performed in this research program. Results from calculations treating bare SWCNTs and calculations which consider CNTs in the presence of NO_2 or NH_3 molecules are compared and graphically presented.

5.1 NO_2 Distance Variation

As stated in the goals of this work, an NO_2 molecule was included in the system in order to simulate the electrical properties of the SWCNT when in proximity with the aforementioned gas molecule. In these modeling calculations, the effect of the distance between an NO_2 molecule and an (8,0) SWCNT was examined. The (8,0) SWCNT has two semi infinite (8,0) SWCNT contacts, with a single NO_2 molecule placed at equilibrium distance from the SWCNT as visualized in figure 5.1. From this position, the molecule was moved further away in subsequent calculations, though its orientation is kept constant, and a 1 V bias was placed over the device region.

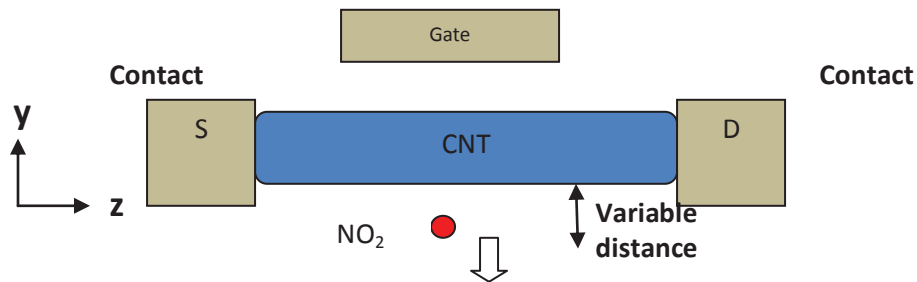


Figure 5.1 Representation of the system for distance variation simulations. S and D stand for source and drain respectively. In these simulations, current was measured at increasing separation distance between the CNT and NO_2 molecule.

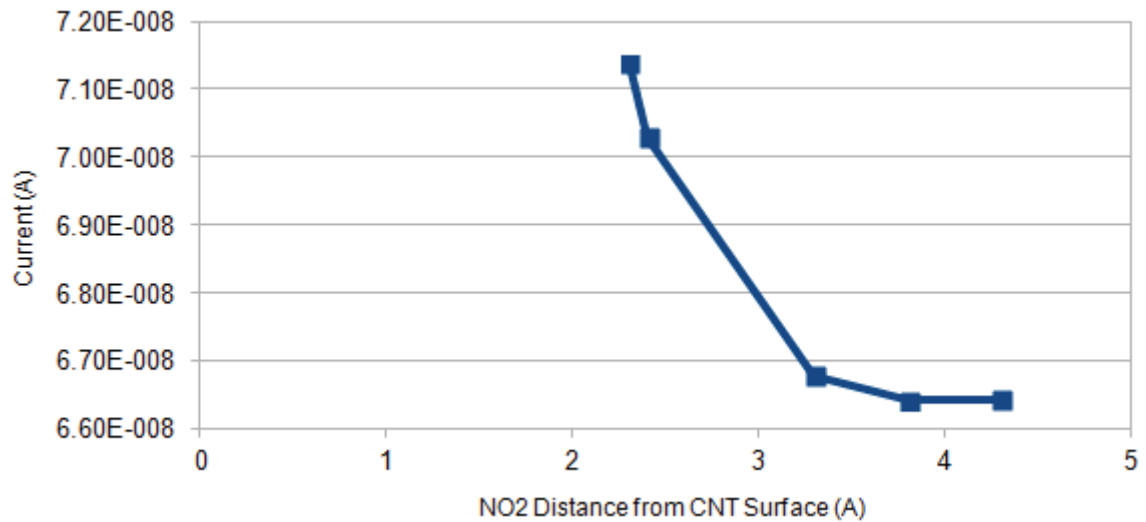


Figure 5.2 Current through a (8,0) SWCNT as a function of the distance of distance of NO₂ molecule from surface. The equilibrium distance for the molecule is 2.3 Angstroms

The results of this investigation can be observed in Fig 5.2. The figure shows that conduction is highest when the NO₂ molecule is at the equilibrium distance of 2.3 angstroms from the SWCNT surface. The current rapidly falls as the NO₂ molecule is moved away, with the influence of the NO₂ molecule no longer being felt at a distance of approximately 3.8 Angstroms. This increase in conductivity follows the expected results from the aforementioned literature of the conductivity of a p-type semiconductor SWCNT when exposed to the hole donating, NO₂ molecule. To better examine what the majority charge carrier in the system is, modeling runs involving a planar gate were carried out.

5.2 Gate Potential Variation

In this configuration, a single (8,0) SWCNT formed the device region with semi-infinite (8,0) SWCNT source and drain contacts, as seen in figures 3.1 and 5.1. The drain voltage was set to 0.1 V for all runs with the source being grounded. A planar gate was also included at a

distance of 7 Angstroms from the center axis of the SWCNT, which was about 3.86 Angstroms from the closest point of the SWCNT. The potential of this gate was varied widely from -20 to 0 V. The NO₂ doped runs contained one NO₂ molecule at the approximate midpoint of the device region, on the bottom side of the CNT (opposite the gate) at a distance of 2.18 Å from nitrogen to carbon atom on the surface (see fig 5.1 and 5.3). The CNT lays in the z direction, with the planar gate parallel to the x-z plane, and above the CNT (see fig 5.1). The NH₃ doped runs contain an NH₃ molecule at the same approximate position along the CNT as the NO₂ molecule in the NO₂ doped runs, but located at its equilibrium distance of 3.67 Å from the surface. A visualization of the NH₃ or NO₂ doped system is shown below in figure 5.3.

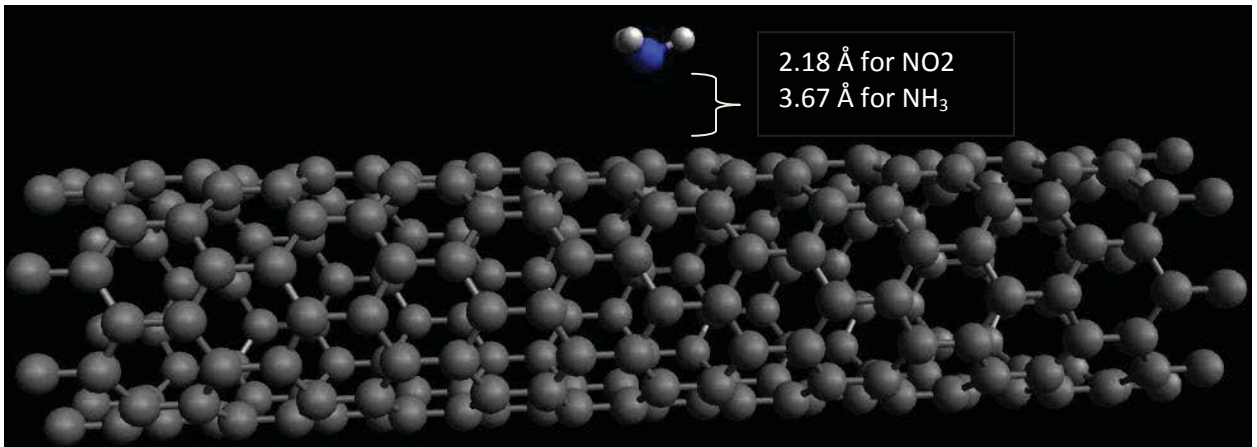


Figure 5.3. Visualization of either NH₃ or NO₂ doped system.

The results obtained (see figure 5.4) demonstrate the expected behavior of an n-type semiconductor. From the figure, it is observed that the current flow rapidly increases with increasing gate voltage for $V_{\text{gate}} > -7$ V, as the lowering of energy bands brought about by the positive potential makes the conduction band more accessible for conduction with electrons as majority charge carrier. For $V_{\text{gate}} < -7$ V, decreasing gate voltage leads to a slow increase in conduction, as rising energy levels lead to more holes in the valence band. Being able to conduct

with both majority charge carriers without having to heavily gate the system suggests the system is capable of acting like an ambipolar semiconductor [48].

The shape of the doped NH_3 curve compares nicely to the annealed, n-type CNTs studied by Avouris et al [20], as shown in figure 2.5. Here, a large increase in conductivity under positive gate voltage is seen. The figure also shows that one dopant molecule of different gases is not enough to completely change the characteristic of these CNTs. Figure 5.4 also displays that the simulated CNTs seem to show a better relative conduction outcome at negative gate voltages than those in Avouris et al's experiment. This could be due to the CNT contacts considered in the present work. The ones used in the Avouris et al's study were based on metal, while the CNT contacts used here are likely closer to the middle of the device bandgap.

Comparing the NO_2 and NH_3 doped results, the expected differences can be observed. The NO_2 displays (due to the hole donation from the NO_2 molecule) lower conduction at positive gate voltages, and higher conduction at more negative gate voltages as compared to the electron donating NH_3 molecule.. This outcome agrees at some degree with Kong's et al [19] results. Both studies show that NO_2 is functioning as a hole donating group, while the NH_3 function as an electron donating group. In the case of the CNT- NO_2 doped system, it seems that this electrical profile is not fully developed into a typical p-type behavior, as it has been reported by Kong et al [19]. However; the results published by Kong et al. were based experiments performed in the presence of oxygen. A physical effect that has been studied by Avouris et al [20]. Indeed, it is expected that the incorporation of O_2 in the system, would result in a typical p-type profile when doping the nanotube with nitrogen dioxide Figure 5.4 also shows that the bare CNT simulations display higher current flow than the doped CNTs at the -10 to 0 gate voltage range. This differs from the Kong et al study (where the bare CNT demonstrated properties between those exposed to the NO_2 and NH_3), probably due to additional scattering

caused by the dopant molecules, a feature that a defect-free bare CNT would not have. The difference in values between the dissimilar doped CNTs also was not as large as in Kong et al and Avouris et al's studies, though this is likely due to only a single dopant molecule used in each case.

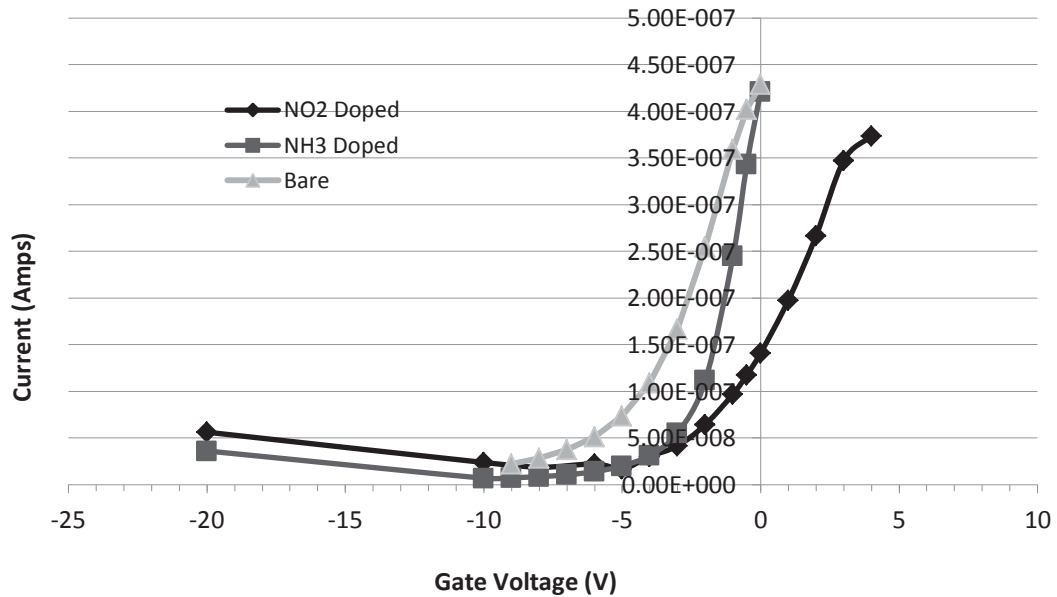


Figure 5.4. Effect of Gate Variation on Current flow through (8,0) CNT. NO₂ Doped CNT shows lowest conduction under positive gate voltage, and highest under negative gate voltage due to hole donation.

5.3 Effects of NO₂ and NH₃ on the Conductivity of CNTs

In the following simulations, a (8,0) SWCNT with semi-infinite SWCNT contacts was placed in an environment with a -7 V planar gate. Modeling runs with varying bias voltages were then conducted with just the SWCNT present, and with a single molecule of NH₃ or NO₂ located approximately at the center of the device region, at distances 3.67 Å and 2.18 Å, respectively, from the CNT surface. The results are shown in figure 5.5.

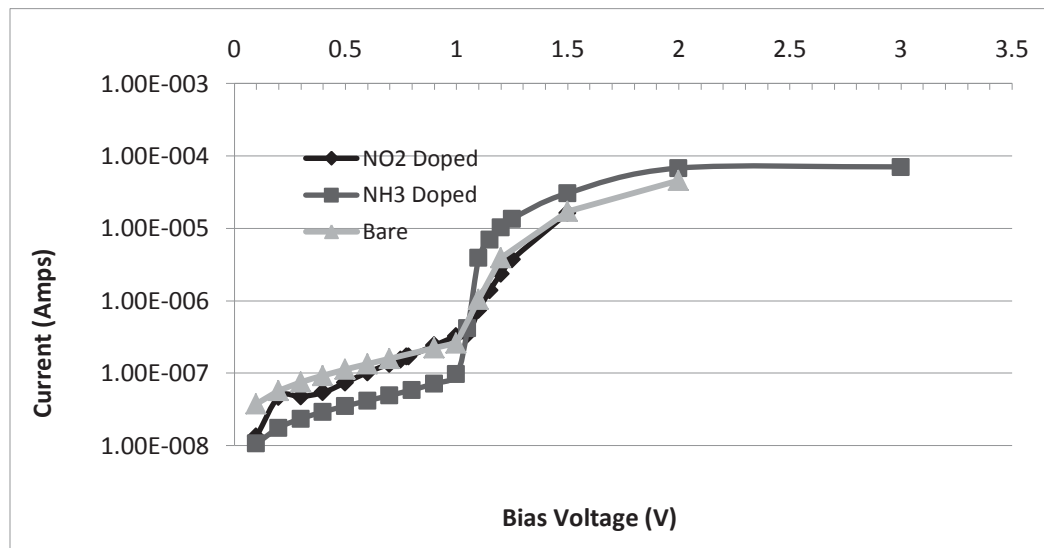


Figure 5.5 Current through an (8,0) SWCNT as a function of bias voltage in the presence of a -7 V planar gate. The presence of NO₂ improves conductivity, while NH₃ slightly reduces it, until a switch to electron charge carrier conduction at 1 V bias.

From the results shown in figure 5.5, it can be seen that the NO₂ doped CNT has higher current flow at low bias than the NH₃ doped CNT, with both increasing slowly. This agrees with the results of Kong et al [19], demonstrating n type semiconductor behavior, though again, the difference between differently doped CNTs is not as large. In contrast, Kong et al's work differs from this study in the case where the bare CNT exhibits slightly higher current flow than the NO₂ doped CNT throughout the studied bias range. However, at around 1 V bias, the NH₃ doped CNT has a sharp increase in current flow while the NO₂ doped and bare CNTs have a much smaller increase. At this point, electrons are able to more easily access the conduction band, causing a switch to electrons being majority charge carrier once again, leading to results similar to those found in Avouris et al [20]. Also, at this point, the NH₃ doped CNT quickly reaches a maximum current, while the NO₂ doped approaches it more slowly due to having less free electron charge carriers.

In summary, the results for sensing here obtained match qualitatively to those reported in the literature. When functioning as a pseudo p-type semiconductor, the NO₂ doped CNTs demonstrated higher conductivity at low gate voltages, with the reverse being true when the CNT was functioning as an n-type semiconductor. The bare CNTs, however, do not lay at the expected values between that of the doped CNTs. Instead, it demonstrates a conductivity that was higher than both doped CNTs, other than NH₃ doped CNTs at high bias voltage. A possible reason for this is that the dopant molecules may interfere somewhat with the otherwise nearly ballistic transport in the defect-free CNTs. Increased number of dopant molecules may cause enough of an increase or decrease in charge carrier to have the bare CNT conductivity be between that of the two kinds of doped CNTs, as well as causing a larger difference in conductivity of differently doped CNTs as observed in studies such as Kong et al and Avouris et al [19, 20]. Exact quantitative comparisons of results obtained and literature are difficult due to the conditions that were modeled, imperfections often present in real CNTs, and not enough information given in many literature sources to exactly recreate the experiment conditions.

6. Conclusions

This work examined the use of DFTB+NEGF modeling for simulating the sensing properties of CNTs. The DFTB+NEGF modeling seems to appropriately model the behavior of an individual SWCNT exposed to either NO_2 or NH_3 molecules under vacuum conditions where the SWCNT is acting as an n-type semiconductor between semi-infinite SWCNT contacts. The presence of a single molecule of NO_2 or NH_3 produced noticeable changes to current flow and behavior in the presence of gate potentials. These changes then rapidly vanished as the molecules were moved further from the CNT surface.

It was observed that the current of the modeled CNTs showed expected n-type semiconductor behavior at gate voltages greater than -5 V. This is related to the lowering of the conduction bands brought about by the positive potential. In this region, exposure to NH_3 , an electron donating molecule, caused an increase in current flow while exposure to NO_2 caused an opposite effect.

At gate voltages lower than -5 V, holes seem to be the majority charge carrier and p-type semiconductor properties are observed, with exposure to NO_2 , a hole donating molecule, causing an increase in current flow while NH_3 has an opposite effect. Higher bias voltages of greater than 1 V cause a return to n-type behavior, however.

While quantitative comparison to experimental results is difficult, due to the specifics of the modeled situation, such as a vacuum and the CNT contacts here investigated, results with respect to NO_2 and NH_3 exposure qualitatively match the expected results. At low bias and gate voltages, modeling can be performed in relatively short time. However, larger bias (greater than 3 V in the single SWCNT case), as well as large systems such as multiple CNTs that are not periodic, can make modeling calculations take significantly longer. These times can be reduced however, by loading initial charge distributions from lower bias runs and dividing the region into

more layers. Nonetheless, the smaller bias should be more than sufficient for acquiring an initial understanding of how SWCNTs electrical properties change upon exposure to other molecules, demonstrating the established sensing properties of CNTs. In conclusion, this work recommends further use of this procedure. This modeling scheme could easily be used to examine more complex configurations, such as metal contacts, increased number of dopant molecules, and more complex dopant molecules.

References

- [1] Iijima, S. Helical microtubules of graphitic carbon. *Nature*. 1991, 354, 56–58.
- [2] Koskinen, Pekka. "Computational Modeling of Carbon Nanotubes." Web. 6 May 2015.
<https://www.jyu.fi/fysiikka/opiskelu/tyoosasto/Modeling_of_C_nanotubes.pdf
- [3] Rafiee, Roham, & Pourazizi, Reza. (2014). Evaluating the influence of defects on the young's modulus of carbon nanotubes using stochastic modeling. *Materials Research, 17*(3), 758-766. Epub May 30, 2014. Retrieved June 24, 2015, from http://www.scielo.br/scielo.php?script=sci_arttext&pid=S1516-14392014000300031&lng=en&tlng=en. 10.1590/S1516-14392014005000071
- [4] Himpsel, F. Energy Bands Powerpoint. [Online]
uw.physics.wisc.edu/~himpself/Nano/EnergyBands.ppt (accessed June 19,2015)
- [5] Zhao, X.; Liu, Y.; Inoue, S.; Suzuki, T.; Jones, R.; Ando, Y. (2004). "Smallest Carbon Nanotube is 3 Å in Diameter". *Phys. Rev. Lett.* 92 (12): 125502.
- [6] Dumitrică T, Kodambaka S, Jun S; Synthesis, electromechanical characterization, and applications of graphene nanostructures. *J. Nanophoton.* 0001;6(1):064501-1-064501-21. doi:10.1117/1.JNP.6.064501.
- [7] Yongji Gong, Andrew R. Barron, Band Gap Measurement. OpenStax CNX. May 29, 2012
<http://cnx.org/contents/d1c4c0c9-7bcb-4245-b320-6d6fdb3ade9e@1>.
- [8] M K Achuthan K N Bhat (2007). "Chapter 10: Metal semiconductor contacts: Metal semiconductor and junction field effect transistors". *Fundamentals of semiconductor devices*. Tata McGraw-Hill. pp. 475 ff. ISBN 007061220X.
- [9] Ferdows Zahid; Magnus Paulsson; Avik Ghosh; Supriyo Datta (2005), "Introduction to Molecular Conduction," <https://nanohub.org/resources/8>.
- [10] Field effect Transistors. *Nanointegris*. [Online]
<http://www.nanointegris.com/en/transistors>

- [11]_Alejandro Strachan (2011), "Tutorial 1: Atomistic Material Science - ab initio simulations of materials," <http://nanohub.org/resources/11917>.)
- [12] Hohenberg, P.; Kohn, W. (1964). "Inhomogeneous Electron Gas". *Physical Review* **136** (3B): B864. Bibcode:1964PhRv..136..864H. doi:10.1103/PhysRev.136.B864
- [13] A Pecchia, L Salvucci, G Penazzi, and A Di Carlo. Non-equilibrium green's functions in density functional tight binding: method and applications. *New J Phys*, 10:065022, 2008.
- [14] H. Salehi and K. Gharbavi, "Ab Initio Study of Electronic Properties of a Armchair (7,7) Carbon Nanotube," *Advances in Materials Physics and Chemistry*, Vol. 2 No. 3, 2012, pp. 159-162. doi: 10.4236/ampc.2012.23024.
- [15] Erkan Tetik, Faruk Karadağ, Muharrem Karaaslan, and İbrahim Çömez, "The Electronic Properties of the Graphene and Carbon Nanotubes: Ab Initio Density Functional Theory Investigation," *ISRN Nanotechnology*, vol. 2012, Article ID 416417, 7 pages, 2012. doi:10.5402/2012/416417
- [16] C. Nirmala Louis, Sr. Gerardin Jayam and A. Amal Raj. Band structure, density of states and superconductivity of adsorbed titanium chains on (8,8) and (14,0) carbon nanotubes. *Materials Physics and Mechanics*, 2010, 10, 72-81.
- [17] N Kuganathan. *Electronic Properties of Graphite and Single Walled Carbon Nanotubes- A DFT Study*. The Internet Journal of Nanotechnology. 2009 Volume 3 Number 2.
- [18] Materials Science Products. (n.d.). Retrieved May 1, 2015, from <http://www.sigmaaldrich.com/materials-science/material-science-products.html?TablePage=16376687>
- [19] Nanotube Molecular Wires as Chemical Sensors. Jing Kong, Nathan R. Franklin, Chongwu Zhou, Michael G. Chapline, Shu Peng, Kyeongjae Cho, and Hongjie Dai. *Science* 28 January 2000: **287** (5453), 622-625. [DOI:10.1126/science.287.5453.622]

- [20] Carbon Nanotube Inter- and Intramolecular Logic Gates. V. Derycke, R. Martel, J. Appenzeller, and Ph. Avouris. *Nano Letters* 2001 1 (9), 453-456 DOI: 10.1021/nl015606f
- [21] Abadir, G.B.; Walus, K.; Turner, R.; Pulfrey, D.L., "Effect of Single-Biomolecule Adsorption on the Electrical Properties of Short Carbon Nanotubes," *Nanotechnology*, 2008. *NANO '08. 8th IEEE Conference on*, vol., no., pp.230,232, 18-21 Aug. 2008 doi: 10.1109/NANO.2008.75
- [22] Qi, P. Vermesh, O. Greco, M. Javey, A. Wang, Q. Dai, H. Toward Large Arrays of Multiplex Functionalized Carbon Nanotubes for Highly Sensitive and Selective Molecular Detection. *Nano Lett.* 2003, 3 (3), 347-351.
- [23] T. Someya, J. Small, P. Kim, C. Nuckolls, and J. T. Yardley, "Alcohol vapor sensors based on single-walled carbon nanotube field effect transistors," *Nano Letters*, vol. 3, no. 7, pp. 877-881, 2003
- [24] Gong S., Zhu Z.H., E. I. Haddad, 'Modeling Electrical Conductivity of Nanocomposites by Considering Carbon Nanotube Deformation at Nanotube Junctions', *Journal of Applied Physics*, Vol. 114, p.074303, 2013. DOI: 10.1063/1.4818478
- [25] Allaouia, A., Hoab, S. V., Evesquea, P., Bai, J.: Electronic transport in carbon nanotube tangles under compression: The role of contact resistance. *Scripta Mater.* 61, 628-631 (2009)
- [26] B. Aradi, B. Hourahine, and Th. Frauenheim. DFTB+, a sparse matrix-based implementation of the DFTB method. *J. Phys. Chem. A*, 111(26):5678, 2007.
- [27] M. Elstner, D. Porezag, G. Jungnickel, J. Elsner, M. Haugk, T. Frauenheim, S. Suhai, and G. Seifert. Self-consistent-charge density-functional tight-binding method for simulations of complex materials properties. *Phys. Rev. B*, 58:7260, 1998.
- [28] C. Köhler, T. Frauenheim, B. Hourahine, G. Seifert, and M. Sternberg. Treatment of collinear and noncollinear electron spin within an approximate density functional based method. *J. Phys. Chem. A*, 111(26):5622, 2007.

- [29] Q. Cui, M. Elstner, T. Frauenheim, E. Kaxiras, and M. Karplus. Combined self-consistent charge density functional tight-binding (scc-dftb) and charmm. *J. Phys. Chem. B*, 105:569, 2001.
- [30] M. Elstner, P. Hobza, T. Frauenheim, S. Suhai, and E. Kaxiras. Hydrogen bonding and stacking interactions of nucleic acid base pairs: a density-functional-theory based treatment. *J. Chem. Phys.*, 114:5149, 2001
- [31] B. Hourahine, S. Sanna, B. Aradi, C. Köhler, T. Niehaus, and Th. Frauenheim. Self-interaction and strong correlation in DFTB. *J. Phys. Chem. A*, 111(26):5671, 2007.
- [32] Y. Yang, H. Yu, D. York, Q. Cui, and M. Elstner. Extension of the self-consistent-charge density-functional tight-binding method: Third-order expansion of the density functional theory total energy and introduction of a modified effective coulomb interaction. *J. Phys. Chem. A*, 111:10861, 2007.
- [33] Felix Bloch (1928). "Über die Quantenmechanik der Elektronen in Kristallgittern". *Z. Physik* 52: 555–600. Bibcode:1929ZPhy...52..555B. doi:10.1007/BF01339455.
- [34] J. C. Slater and G. F. Koster, *Phys. Rev.* 94, 1498 (1954).
- [35] On the Non-Orthogonality Problem Connected with the Use of Atomic Wave Functions in the Theory of Molecules and Crystals Lowdin, Per-Olov, *The Journal of Chemical Physics*, 18, 365-375 (1950), DOI:<http://dx.doi.org/10.1063/1.1747632>
- [36] T. Frauenheim, G. Seifert, M. Elstner, Z. Hajnal, G. Jungnickel, D. Porezag, S. Suhai, and R. Scholz, *A self-consistent charge density-functional based tight-binding method for predictive materials simulations in physics, chemistry and biology*, *Physica Status Solidi (b)* **217**, 41 (2000)
- [37] R. Pariser, *J. Chem. Phys.* 24, 125 (1956).
- [38] J.F. Janak, *Phys. Rev. B* 18, 7165 (1978).
- [39] Elstner, Marcus. "Introduction to DFTB." 28 July 2006. Web. 5 May 2015.
http://www.mcc.uiuc.edu/summerschool/2006/presentations/Elstner_DFTB.pdf

- [40] D. Porezag, Th. Frauenheim, Th. Köhler, G. Seifert, and R. Kaschner, *Phys. Rev. B* **51**, 12947 (1995).
- [41] J. P. Perdew and A. Zunger, *Phys. Rev. B* **23**, 5048 (1981).
- [42] Y. Xue, S. Datta and M. A. Ratner, "First-principles based matrix Green's function approach to molecular electronic devices: general formalism," *Chemical Physics*, Vol. 281, No. 2-3, pp. 151-170, 2002.
- [43] Nanotube Transistors, Carbon Nanotubes, Jose Mauricio Marulanda (Ed.), ISBN: 978-953-307-054-4, *InTech*, DOI: 10.5772/39424. Available from: <http://www.intechopen.com/books/carbon-nanotubes/fundamental-physical-aspects-of-carbon-nanotube-transistors>
- [44] TubeGen 3.4 (web-interface, <http://turin.nss.udel.edu/research/tubegenonline.html>), J. T. Frey and D. J. Doren, University of Delaware, Newark DE, 2011]
- [45] Hanwell, M. D.; Curtis, D. E.; Lonie, D. C.; Vandermeersch, T.; Zurek, E.; Hutchison, G. R. Avogadro: an advanced semantic chemical editor, visualization, and analysis platform. *J. Cheminform.* 2012, 4, 17.
- [46] DFTB+. Web. 24 Apr. 2015. <<http://www.dftb-plus.info/>>.
- [47] DFTB. Web. 24 Apr. 2015. <<http://www.dftb.org/parameters/download/>>
- [48] Yung-Fu Chen and M. S. Fuhrer, "Electric-field dependent charge-carrier velocity in semiconducting carbon nanotubes," *Phys. Rev. Lett.* **95**, 236803 (2005).